Supplementary information for

Electrocatalytic conversion of CO_2 to glycerol through by nanoconfinement

Jianxin Wang[1,2,8], Haozhe Zhang[1,2,8], Fakhrul Hasan Bhuiyan[3], Shichen Guo[1,4], Chukwunwike O. Iloeje[4], Yuzi Liu[5], Zhenzhen Yang[1], Yuanlong Bill Zheng[2], Xudong Xiao[5,6], Moon Park[1], Tongchao Liu[1], Jing Wang[1,2], Tao Xu[6,*], Alvaro Vazquez Mayagoitia[3], Ying Shirley Meng[2,7,*], Di-Jia Liu[1,2,*]

[1]Chemical Sciences and Engineering Division, Argonne National Laboratory, Lemont, Illinois 60439, United States

[2]Pritzker School of Molecular Engineering, The University of Chicago, Chicago, Illinois 60637, United States

[3]Computational Science Division, Argonne National Laboratory, Lemont, Illinois 60439, United States

[4]Energy Systems and Infrastructure Assessment Division, Argonne National Laboratory, Lemont, Illinois 60439, United States

[5]Center for Nanoscale Materials, Argonne National Laboratory, Lemont, Illinois 60439, United States

[6]Department of Chemistry and Biochemistry, Northern Illinois University, DeKalb, Illinois 60115, United States

[7]Energy Storage Research Alliance, Argonne National Laboratory, Lemont, Illinois 60439, United States

[8]These authors contributed equally.

*Corresponding authors. djliu@anl.gov, shirleymeng@uchicago.edu, txu@niu.edu

This PDF file includes:

Supplementary Methodes

1. Catalyst Structural Characterization
2. Catalyst Synthesis
3. Electrocatalytic Performance Measurements
4. Advanced Machine Learning

Supplementary Figures. 1-35

Supplementary Tables 1-7

Supplementary References

Table of Contents

Supplementary Methodes

1. Catalyst Structural Characterization:

BET specific surface area (S_{BET}). The Brunauer–Emmett–Teller (BET) specific surface area of the sample was determined using its N_2 adsorption isotherm, measured on a Micromeritics ASAP™ 2020. Prior to the measurement, approximately 100 mg of sample was degassed under vacuum at 150 °C for 12 h. To better reflect the carbon surface property after caustic ALM synthesis, we pre-washed these carbons with concentrated LiOH solution before degasing and drying step. A total of 30 data points were selected across the N_2 isotherm to construct the BET plot of $\frac{P}{V(P_o-P)}$ versus $\frac{P}{V}$, where V is the volume of N_2 adsorbed (cm^3 STP g^{-1}), P is the equilibrium pressure, and P_0 is the saturation pressure. Utilizing the linear portion of this plot, the slope ($m = \frac{C-1}{V_m C}$) and intercept ($Y_{INT} = \frac{1}{V_m C}$) were obtained, C is the BET constant. This allows the monolayer adsorption volume V_{m} to be determined as $\frac{1}{m+Y_{\mathrm{INT}}}$. The S_{BET} was derived using the formula[1]:

$$S_{\mathrm{BET}} = \frac{V_m \cdot N_A \cdot \sigma}{V_m^{\mathrm{mol}}} \times 10^{-18}$$

where N_A is Avogadro's number, $V_m^{\mathrm{mol}} = 22414\ cm^3\ \mathrm{mol}^{-1}$ is the molar volume of an ideal gas at STP, and $\sigma = 0.162\ \mathrm{nm}^2$ is the molecular cross-sectional area of N_2. The factor 10^{-18} converts from nm^2 to m^2. The resulting S_{BET} is reported in units of m^2 g^{-1}.

2D Nonlocal density functional theory (2D-NLDFT) porosity distribution. From the N_2 adsorption isotherm obtained at 77 K, the pore size distribution of the sample was extracted using the 2D-NLDFT method. 2D-NLDFT considers the interaction between the N_2 adsorptive and the adsorbent, including the molecular size and geometry of the adsorptive species. The contribution of each pore configuration is weighted by its fraction in the pore distribution function of the sample. This relationship is expressed by[2]:

$$Q(p) = \iint q(p, H, \varepsilon)\, f(H, \varepsilon)\, dH d\varepsilon$$

where $Q(p)$ denotes the experimentally measured adsorption amount at relative pressure p. The function $q(p, H, \varepsilon)$ represents the theoretical adsorption within an idealized pore of width H and surface potential ε, as obtained from 2D-NLDFT calculations or molecular simulations. The pore distribution function $f(H, \varepsilon)$ describes the fraction of pores in the sample that possess a given size H and and surface energy ε. The integration is carried out over all possible combinations of pore size and surface heterogeneity $(dHd\varepsilon)$ to reconstruct the total adsorption isotherm.

We named our carbon supports based on conventional porosity nomenclature, with "micro" defined as the pores with diameters < 2 nm, "meso" defined with pore width between 2 nm to 50 nm and "mix" as the support mixed with pores in micro-, meso-, as well as macropores (diameter > 50 nm).

CO_2 sorption isotherm. CO_2 sorption isotherms were measured a Micromeritics ASAP^{TM} 2020 instrument at 0 °C and 24 °C with approximately 100 mg of sample. Prior to analysis, the samples were degassed under vacuum at 150 °C for 12 hours to remove physisorbed species. The resulting isotherm comprised 73 adsorption data points and 49 desorption data points, spanning a relative pressure range from 0.001 to 1. Each data point was recorded after a minimum equilibration time of 3 minutes to ensure measurement stability. The relative pressure was precisely controlled throughout the adsorption-desorption process, enabling accurate acquisition of sorption behavior across the full pressure range.

Thermodynamic parameters of CO_2 adsorption. The calculation of the enthalpy of adsorption $(-\Delta H_{\mathrm{ads}})$ and entropy of CO_2 adsorption $(-\Delta S_{\mathrm{ads}})$ using the van 't Hoff plot after dual-site Langmuir (DSL) fit method from CO_2 adsorption isotherms at 273.15 K and 297.15 K, respectively. The formula for the DSL model is represented as[3]:

$$q_{\mathrm{CO_2}} = \frac{q_{m_1} b_1(T) P}{1 + b_1(T) P} + \frac{q_{m_2} b_2(T) P}{1 + b_2(T) P}$$

where $q_{\mathrm{CO_2}}$ represents the amount of CO_2 adsorbed per unit mass of the adsorbent; q_{m_1} and q_{m_2} denote the saturated adsorption capacities at the 1st and 2nd types of CO_2 adsorption sites, respectively; $b_1(T)$ and $b_2(T)$ are the Langmuir adsorption equilibrium constants corresponding to these adsorption sites, indicating the affinity of the adsorbent for the CO_2; P is the adsorption equilibrium pressure. From the fitting results, extract b_1 and b_2 at both 0 °C and 24 °C. These are the equilibrium constants that will be used for the van't Hoff analysis.

The extraction of site-specific adsorption enthalpies and entropies using the van't Hoff plot is represented by the following equation[4]:

$$\ln K_{\mathrm{eq}} = \ln b_i = -\frac{\Delta H_{\mathrm{ads},i}}{RT} + \frac{\Delta S_{\mathrm{ads},i}}{R}$$

where K_{eq} is the CO_2 adsorption equilibrium constant, b_i are the Langmuir adsorption equilibrium constants extracted from DSL fitting.

In a van't Hoff plot, the inverse of the temperature $\frac{1}{T}$ is plotted on the X-axis, and the natural logarithm of the equilibrium constant K_{eq} on the Y-axis. The slope and intercept of the resulting line can be directly used to calculate $-\Delta H_{\mathrm{ads}}$ and $-\Delta S_{\mathrm{ads}}$:

$$-\Delta H_{\mathrm{ads}} = R \times \mathrm{slope}$$

$$-\Delta S_{\mathrm{ads}} = -R \times \mathrm{intercept}$$

To validate the accuracy of ΔH_{ads} derived from the van't Hoff analysis, an independent calculation was conducted using the Clausius-Clapeyron equation. The adsorption enthalpy at a given loading was obtained from the pressures corresponding to the same amount of CO_2 adsorbed at two different temperatures, based on the isotherms fitted using the DSL model[5]:

$$ln\left(\frac{p_2}{p_1}\right) = -\frac{\Delta H_{\mathrm{ads}}}{R}\left(\frac{1}{T_2} - \frac{1}{T_1}\right)$$

where p_1 and p_2 are the equilibrium pressures corresponding to a fixed adsorption amount at temperatures T_1 and T_2 respectively, and R is the gas constant. The $-\Delta H_{\mathrm{ads}}$ values obtained from this method were found to be in good agreement with those derived from the van't Hoff analysis, confirming the reliability of the extracted thermodynamic parameters.

Electron paramagnetic resonance (EPR). The EPR data were recorded using a (Elexsys E500 CW-EPR) X-band continuous wave (CW) EPR spectrometer at the Center for Nanoscale Materials (CNM), Argonne National Laboratory (ANL). A Mercury iTC temperature controller (Oxford Instruments) was used for low-temperature measurements. The entire system was operated using

Bruker Xenon software. The X-band frequency was 9.365 GHz, the microwave power was set to 2 mW, and the modulation amplitude (100 kHz) was 10 G. The temperature for the EPR measurement was set to 20 K.

Raman spectroscopy of CO_2 adsorption. The adsorption of CO_2 was monitored using shell-isolated nanoparticle-enhanced Raman spectroscopy (SHINERS) recorded on a Horiba Jobin-Yvon LabRam HR800 confocal Raman system. Excitation was provided by a 532 nm Nd:YAG (neodymium-doped yttrium aluminum garnet) laser, coupled with an 1800 gr mm^{-1} sinusoidal groove holographic grating. The laser power density on the sample was approximately 0.05 mW μm^{-2}, as measured by a laser power meter. Raman spectra of CO_2 adsorbed on the adsorbent were acquired over 20 scans with an integration time of 10 s per scan. A Leica long working distance objective (50× magnification, numerical aperture NA = 0.55, working distance = 8 mm) was used to focus the laser onto the sample and collect the Raman scattered light. Spectrometer calibration was conducted before each measurement using a Si standard to ensure measurement accuracy. For CO_2 adsorption sample preparation, 5 mg of the adsorbent was first dispersed in 1 mL of methanol and ultrasonicated for 1 h. Then, 40 μL of the resulting dispersion ink was mixed with 40 μL of concentrated SHIN solution containing Au@SiO_2 core–shell nanoparticles (55 nm Au core diameter, 3 nm SiO_2 shell thickness) uniformly dispersed in water. The Au@SiO_2 core-shell nanoparticles exhibited a localized surface plasmon resonance (LSPR) maximum peak at λ_{max} = 539 nm. The mixture was then deposited onto a 0.2 cm^2 carbon paper and vacuum dried for 3 hrs. Subsequently, the prepared sample was placed in a 20 mL vial filled with CO_2, sealed, and stored overnight at 4 °C. Upon removal from refrigeration and temperature equilibration to ambient conditions, the sample was subjected to SHINERS measurements.

X-ray fluorescence analysis (XRF). The weight percentage of Cu in Cu/C catalysts was quantified by XRF (Rigaku NEX CG Energy Dispersive XRF) using Cu and Mo targets. To ensure the precision and accuracy of the Cu loading measurements, a calibration curve was established using fluorescence signals from Cu K-edge over a series of CuO/C standard samples with varying Cu loadings. By comparing the Cu signal intensity in the catalyst samples to that of the standards, the Cu content in the Cu/C-*x* samples was subsequently determined.

Fourier transform infrared spectroscopy (FTIR). A homogeneous mixture was prepared by thoroughly grinding the 1 mg of catalyst with 10 mg of dried KBr. The mixture was subsequently pressed under high pressure to form a transparent pellet. FTIR spectra were recorded using a Bruker Vector 22 FTIR spectrometer. The sample pellet was placed in the sample holder, and infrared radiation was passed through the pellet. Absorption spectra were collected across a range of frequencies. From these data, molecular vibrational modes were determined, allowing identification of chemical composition and functional groups.

X-Ray photoelectron spectroscopy (XPS). XPS measurements were performed on a Physical Electronics PHI 5000 VersaProbe II system with Al K_α radiation (1486.6 *e*V) under fixed analyzer transmission mode. For calibration, the XPS spectra were aligned to the C 1s peak of adventitious carbon at 284.8 *e*V. Spectra were collected with a pass energy of 10 *e*V and an energy step size of 0.1 *e*V.

Powder X-ray diffraction analysis (PXRD). PXRD patterns were collected at ambient temperature using a Bruker D8 Advance diffractometer with Cu K_α radiation (λ = 1.5418 Å, 40 kV, 40 mA). The powdered samples were mounted on a zero-background silicon holder. The diffraction data were acquired over a 2θ range of 10 to 90°, with a step size of 0.005° and a dwell time of 1 s per step.

High-magnification high-angle annular dark-field scanning transmission electron microscope (HAADF-STEM). SAs were visualized using HAADF-STEM at the Center for Nanoscale Materials (CNM) at Argonne National Laboratory (ANL). The instrument employed was a probe-corrected Thermo Fisher Spectra 200, equipped with a 200 kV cold field emission gun and a Cs probe corrector, facilitating HAADF imaging with sub-0.1 nm resolution. Some TEM images were obtained on Analytical PicoProbe Electron Optical Beam Line at Argonne National Laboratory which is the prototype of the ThermoFischer Scientific Spectra 300 Ultra X/Illiad analytical electron microscope. Sample preparation involved dispersing the sample in methanol, followed by ultrasonic treatment and deposition onto ultra-thin carbon film-coated gold TEM grids (TED PELLA, Inc.). The gold grids were subsequently dried under vacuum at 60 °C.

X-ray absorption measurements (XAS). All XAS data were collected at the Cu K-edge (~9659 eV) at beamline 7-BM of the National Synchrotron Light Source II at Brookhaven National Laboratory, NY. The fluorescence mode is used due to the low loading of Cu. The Cu foil was measured for energy calibration for each scan of the samples. Each measurement was conducted for at least ten scans that were later merged to improve the signal-to-noise ratio.

X-ray absorption near edge structure (XANES) and extended X-ray absorption fine structure (EXAFS) analysis. The normalized, energy-calibrated Cu K-edge XANES spectra were obtained using standard data reduction techniques with Athena and Artemis software[6]. The EXAFS oscillations $\chi(k)$ as a function of photoelectron wave number k was extracted by following standard procedures.

Gas chromatography (GC) analysis. Gaseous products were collected using a gas-tight syringe and analyzed on an Agilent HP 6890N GC system equipped with a packed Hayesep D column. Argon (Praxair, 99.999%) was used as the carrier gas. Calibration was performed using certified standards of H_2, CH_4, C_2H_4, and CO. In chronoamperometric experiments, effluent gases from the cathode chamber were sampled every 2000 s after reaching steady-state and injected into the sampling loop. Each applied potential was repeated three times, and the average of three runs was reported. The separated gas products were detected using a flame ionization detector (FID) coupled with a methanizer (for CO, CH_4, and other hydrocarbons) and a thermal conductivity detector (TCD) for H_2. Calibration curves were constructed using certified gas mixtures with CO_2 dilution via a mass flow controller. Quantification was based on conversion factors derived from calibration curves and the average integrated peak areas.

^{1}H Nuclear magnetic resonance (NMR) Analysis. Liquid product yields, such as glycerol, ethanol, acetate, and other compounds generated during the electrolysis process, were quantified using ^{1}H NMR spectroscopy. Dimethyl sulfoxide (DMSO, 99.9%, Sigma Aldrich) and phenol (99%, Sigma Aldrich) were employed as internal standards. Water peak suppression was achieved through a pre-saturation sequence. Liquid products were recorded on a Bruker Avance III NMR spectrometer operating at 11.7 T (500 MHz ^{1}H). To circumvent issues related to differing T1 values of analytes, all spectra were acquired with the same parameters to ensure complete relaxation and quantification. Detailed acquisition parameters included: time domain data size (TD) of 65536; number of dummy scans (DS) of 2; number of scans (NS) of 32; loop count time domain (TD0) of 1; spectral width (SW) of 19.9899 ppm; sweep width in Hertz (SWH) of 10000.00 Hz; filter width (FW) of 125000.00 Hz; pulse width (pw) of 45°; d1 of 5 s; and d2 of 0 s. A total of 32 scans were centered around the water peak, with baseline variations in the middle of the spectrum corresponding to the position of the suppressed water peak. For NMR sample preparation, 600 μL of the electrolyte sample was mixed with 30 μL of internal standard solution. The internal standard solution was prepared by mixing 14 ml D_2O with 10.0 μL DMSO and 66 mg phenol, equivalent to a D_2O solution of 10 mM DMSO and 50 mM phenol. Standard curves for each product were plotted based on relative peak area ratios.

^{2}H NMR analysis. Dimethyl sulfoxide-*d6* (DMSO-*d6*, 99.9%, Sigma-Aldrich) was used as an internal standard for recording liquid products on a Bruker Avance III NMR spectrometer operating at 11.7T (500 MHz for 2H). To avoid issues arising from analytes having different T1 values, all spectra were acquired using the same spectral parameters to ensure complete relaxation and quantification. The acquisition parameters included a time domain data size (TD) of 131072; dummy scans (DS) of 4; number of scans (NS) of 64; time domain of cycle count (TD0) of 1; spectral width (SW) of 9.9986 ppm; acquisition time (AQ) of 3.2767999; filter width (FW) of 625,000 Hz; receiver gain (RG) of 71.8; dwell time (DW) of 25 μs; oversampling dwell time (DWOV) of 0.025; digital filter decimation rate (DECIM) of 1000; digitizer resolution (DR) of 22; digital-to-analog converter resolution (DDR) of 10; pre-scan delay (DE) of 6.50 μs. Processing parameters included a real data size (SI) of 16384; spectrometer frequency (SF) of 500.25 MHz; low field limit of the spectrum (OFFSET) of 24.69 ppm; spectrum reference frequency (SR) of 0 Hz; spectral resolution (HZpPT) of 1.220703. For NMR sample preparation, 600 μl of the electrolyte sample was mixed with 30 μl of internal standard solution. The internal standard solution was prepared by mixing 14 ml D_2O with 10.0 μl DMSO-*d6*, equivalent to a 10 mM DMSO-*d6* solution in D_2O.

***in-situ* electrochemical shell-isolated nanoparticle-enhanced Raman spectroscopy (EC-SHINERS).** The measurements were conducted using a Renishaw confocal Raman system. Laser excitation was performed using a 785 nm diode laser, coupled with a 1200 gr mm^{-1} sinusoidal groove holographic grating. The power density of the laser at the sample was approximately 0.1 mW μm^{-2}. as measured by a laser power meter. Each Raman spectrum was acquired over 3 scans with an integration time of 30 s per scan. A Nikon water immersion/dipping objective (40× magnification, numerical aperture NA = 0.8, working distance = 3.5 mm) was used to focus the laser onto the sample and collect the Raman scattered light. Spectrometer calibration was conducted before each measurement using a Si standard to ensure measurement accuracy. For working electrode preparation, 5 mg of the adsorbent was first dispersed in 1 mL of methanol and ultrasonicated for 1 h. Then, 40 μL of the resulting dispersion ink was mixed with 20 μL of concentrated SHIN solution containing Au@SiO_2 core–shell nanorods (10 nm radial diameter and 38 nm axial length of Au nanorods core, and 3 nm SiO_2 shell thickness) uniformly dispersed in water. The Au@SiO_2 core-shell nanorods exhibited a LSPR maximum peak at $\lambda_{max} = 785$ nm. The mixture was then deposited onto a 0.2 cm^2 carbon paper and vacuum dried overnight, the sample was subjected to EC-SHINERS measurements. Electrochemical CO_2RR measurements were conducted in a spectroelectrochemical cell fabricated from PEEK material, employing catalyst electrodes, Pt wire, and Ag/AgCl electrode as the WE, CE, and RE, respectively. A CO_2-saturated 0.1 M $KHCO_3$ solution, totaling 20 mL, served as the electrolyte. Throughout the experiment, CO_2 was continuously injected into the solution at a rate of 20 mL min^{-1}. Prior to spectral acquisition, each potential was applied for 1 min to ensure steady-state conditions on the catalyst surface. During the electrochemical process, SHIN acted as a Raman signal "amplifier", with each Au core protected by an electrochemically inert SiO_2 shell, ensuring that the Raman signals originated exclusively from the surfaces of interest.

2. Catalyst Synthesis:

Synthesis of Cu-LiOH precursor. The Cu-LiOH precursor was synthesized within an Ar-filled glovebox where O_2 levels were maintained below 0.3 ppm and H_2O levels below 0.5 ppm, utilizing a procedure analogous to previously reported methods[7,8]. Lithium (2 g, 99.9% trace metals basis, Sigma-Aldrich) was introduced into a zirconium crucible and was heated until a temperature of 320°C, leading to the formation of molten lithium. Subsequently, Cu wires (20 mg, 99.999% trace metals basis, Sigma-Aldrich) were introduced into the molten lithium, and sonication was applied at 320°C for a duration of 3 hours. Upon completion, the molten metal amalgam was promptly poured onto a 316-stainless steel plate for quenching, resulting in an amalgamated Cu–Li formation. Once cooled, the Cu-Li amalgam was removed from the glovebox, processed into sheets, and segmented into smaller strips. Exposure to humidified air at ambient temperature facilitated the gradual transformation of the Cu-Li amalgam into Cu-$LiOH \cdot H_2O$. The Cu-LiOH precursor was finally procured through the decrystallization of Cu-$LiOH \cdot H_2O$ under vacuum drying conditions at 80°C sustained over 24 hours.

Synthesis of carbon-supported Cu catalysts. Various carbon-supported Cu catalysts were synthesized by ball milling the Cu-LiOH precursor with carbon using a planetary ball-mill machine

(PM 100, Retsch®). In a representative procedure, DLC Supra 50 (C_{micro}) weighing 0.2 g and the Cu-LiOH precursor weighing 0.2771 g were combined in a stainless steel ball-mill jar (50 mL, Retsch®) filled with 10 g of zirconia balls (diameter 5 mm, Alfa Aesar). This jar was then subjected to a rotational speed of 500 rotations per minute (rpm) in the planetary ball-mill machine for 1 h. Subsequent to ball milling, the resulting powders were filtered through a membrane filter (0.22 μm pore size, Sigma-Aldrich) using 500 ml of distilled water, facilitating the leaching of LiOH. The residues collected from the membrane filter were then dried under vacuum at 80 °C for 24 h, yielding a catalyst containing 0.4 wt.% of Cu on C_{micro}, denoted as Cu/C_{micro}-0.4. Catalysts with varied Cu loadings on C_{micro}, including 0.2 wt.% (Cu/C_{micro}-0.2), 0.8 wt.% (Cu/C_{micro}-0.8), 1.6 wt% (Cu/C_{micro}-1.6), 3.2 wt.% (Cu/C_{micro}-3.2), and 6.4 wt.% (Cu/C_{micro}-6.4), were synthesized using an analogous methodology. The protocol employed for the preparation of catalysts with diverse Cu loadings on differing carbon supports mirrored the one used for Cu/C_{micro}-0.4. This included catalysts with different Cu contents on Ketjenblack EC-600JD (C_{meso}), specifically 0.4 wt.% (Cu/C_{meso}-0.4), 1.6 wt.% (Cu/C_{meso}-1.6), 6.4 wt.% (Cu/C_{meso}-6.4), as well as catalysts with varying Cu concentrations on Black Pearls® 2000 (C_{mix}), namely 0.4 wt.% (Cu/C_{mix}-0.4), 1.6 wt.% (Cu/C_{mix}-1.6), and 6.4 wt.% (Cu/C_{mix}-6.4).

3. Electrocatalytic Performance Measurements:

Electrode preparation. The catalyst inks were prepared by dispersing 5 mg of catalyst in a solvent mixture, followed by sonication in an ice bath for 1 h. The solvent mixtures of Cu/C_{micro} -*x* series, Cu/C_{mix}-*x* series and Cu/C_{meso}-*x* series catalysts were added with 1ml methanol and 50 mg of Nafion® (5 wt.% in lower aliphatic alcohols and water, Sigma-Aldrich). The ink was then deposited onto carbon paper (CT GDL340, Fuel Cell Store) with an effective area of 1 cm^2. After the solvent had dried, the working electrodes were obtained. For all catalysts, a loading amount of 1 mg was utilized.

Calibration of Ag/AgCl reference electrode and conversion to RHE. Before each electrochemical measurement, the Ag/AgCl reference electrode was calibrated. Calibration was carried out in a standard three-electrode system where polished Pt wires were employed as the working and counter electrodes, with the Ag/AgCl serving as the reference electrode. The 0.1M $KHCO_3$ solution was first prepared and then purged with pure hydrogen gas for 30 minutes to ensure the removal of dissolved oxygen. Subsequently, the RHE was introduced into the solution, and a constant flow of hydrogen gas was maintained over its surface. Electrochemical measurements were then performed in which the potential of the Ag/AgCl electrode relative to the RHE was determined under equilibrium conditions. The open-circuit potential between the Ag/AgCl electrode and the RHE was measured using a potentiostat. The recorded potential difference provided the calibration value for the Ag/AgCl electrode in that specific solution. Upon completion of the calibration, the Ag/AgCl electrode was ready for use in subsequent electrochemical experiments, its potential accurately referenced to the RHE.

Electrochemical measurements for CO_2 reduction. All electrochemical measurements for CO_2 reduction were conducted in an H-Cell. The system comprised three electrodes: a carbon paper loaded with catalyst serving as the working electrode and a double-junction Ag/AgCl electrode as the reference electrode, both positioned in the cathode chamber, and gold employed as the counter electrode in the anode chamber. The cathode and anode were separated by an anion exchange membrane (Selemion, AEM) and each filled with 30 mL of 0.1 M $KHCO_3$ electrolyte. Before each measurement, the Ag/AgCl reference electrode was calibrated using the reversible hydrogen electrode (RHE). Additionally, the H-Cell was equipped with CO_2 inlets and outlets for purging. Prior to CO_2 electrolysis, the cathode and anode chambers were purged with CO_2 (60 mL min^{-1}) for 45 min to achieve a CO_2-saturated 0.1 M $KHCO_3$ solution (pH ≈ 6.8). During the electrolysis, CO_2 gas was continuously fed into the cathode chamber at 30 mL min^{-1} through a gas dispersion tube. After 2000 s at a specified chronoamperometry electrolysis potential, 600 μL of the electrolyte were extracted separately from both the catholyte and anolyte for NMR analysis of the liquid phase products, while the gaseous products were measured using GC.

Chronoamperometry measurements. FE and current density of CO_2RR electrolysis under the constant potential were studied to verify the catalyst stability. Measurements were taken between −0.3 V and −1.0 V under a continuous flow of CO_2 at 60 mL min^{-1} for 2000 s.

Kinetic isotope effect (KIE) experiment: KIE experiment using 0.1 M $KDCO_3$ in D_2O as solution. The KIE ascribes the change of reaction rate constant during proton-couple electron transfer (PCET) reaction such as electrocatalytic reduction of CO_2 to chemicals. It originates from the difference between proton and deuteron in tunneling probabilities due to the overlap of reactant and product proton/deuteron wavefunctions. In our experiment, KIE was measured following the same process as the regular CO_2RR reaction measurement, except that high purity D_2O (99.9 atom% D, Sigma-Aldrich) is used as the solvent instead of H_2O. Briefly, 0.5 g $KDCO_3$ was dissolved in 50 ml D_2O to prepare 0.1M $KHCO_3$ solution. The D_2O based CO_2RR study follows the same procedure as the H_2O based study, and soluble products were analyzed by ^{2}H NMR spectra. KIE in electrocatalytic CO_2RR to given chemical can be described by the ratio in the rate constant of CO_2 reduction in H_2O and D_2O electrolytes. The KIE is calculated using the following formula[9]:

$$\mathrm{KIE} = \frac{k(\mathrm{H})}{k(\mathrm{D})}$$

Where k(H) is the rate constant of the reaction involving proton transfer (H) whereas k(D) is the rate constant of the reaction with deuteron transfer (D). In our study, the amount of chemicals converted through CO_2RR, Mi (i =glycerol, ethanol, formate…) can be calculated by $\mathrm{M}_i = k_i \times [\mathrm{CO}_2] \times \mathrm{t}$, where k_i represents the rate constant for conversion to chemical i, $[\mathrm{CO}_2]$ represents CO_2 concentration, and t represents reaction time. Since we maintained the same test time and CO_2 concentration for the electrocatalytic test in H_2O and D_2O based electrolyte, the KIE for a particular chemical i can simply calculated by the following equation:

$$\mathrm{KIE}_i = \frac{k_i(\mathrm{H})}{k_i(\mathrm{D})}$$

Electrochemical surface area (ECSA) determination. The electric double layer capacitance (EDLC) of a series of Cu/C electrodes was evaluated before electrolysis[10]. This was achieved by measuring CV curves across a range of scan rates (1 to 8 mV s^{-1}) within the non-Faradaic region (0.3 to 0.4 V vs. RHE). All current densities were normalized based on the geometric area of the electrodes. The method involved extracting half the peak current difference at 0.35 V vs. RHE as a function of the scan rate, thus enabling the determination of the slope for each sample. The plotted slope is equal to the EDLC of the measured sample. The ECSA can be calculated using the formula[11]:

$$\mathrm{ECSA} = \frac{C_{\mathrm{dl}}}{C_{\mathrm{s}}}$$

where C_{dl} is the normalizing EDLC obtained from the slope of the $j_{\text{capacitance}}$ vs. scan rate plot, and C_{s} is the specific capacitance of the material (60 μF cm^{-2}, the specific capacitance value of a smooth surface).

Tafel plot. The Tafel plot was constructed based on the logarithmic relationship between the steady-state partial current density (j_i) and the overpotential (η)[12], as obtained from chronoamperometric measurements. For a given product such as j_{glycerol}, the data were fitted linearly in the low-overpotential region to extract the Tafel slope. The overpotential was calculated as $\eta = E^{\circ} - E$, where E denotes the equilibrium potential.

Thermodynamic potential of glycerol formation. The standard Gibbs free energy change for CO_2 reduction to glycerol was calculated based on the following reaction:

$$3\ CO_2\ (g) + 14\ H^+ + 14\ e^- \rightarrow C_3H_8O_3\ (l) + 3\ H_2O\ (l)$$

$$\Delta G^{\circ}_{\text{glycerol}} = \sum \Delta G^{\circ}_{f\ \text{products}} - \sum \Delta G^{\circ}_{f\ \text{reactants}}$$

$$= \left[\Delta G^{\circ}_{f\ C_3H_8O_3} + 3\Delta G^{\circ}_{f\ H_2O}\right] - 3G^{\circ}_{f\ CO_2}$$

$$= [-438.52\ \mathrm{kJ\ mol^{-1}} + 3\ (-237.14\ \mathrm{kJ\ mol^{-1}})] - 3\ (-394.39\ \mathrm{kJ\ mol^{-1}})$$

$$= 33.23\ \mathrm{kJ\ mol^{-1}}$$

The thermodynamic potential of glycerol for CO_2RR *vs.* RHE was calculated using the Nernst equation, with consideration of the experimental conditions of pH 6.8 and temperature of 23 °C, and based on the calculated potentials *vs.* SHE:

$$E^{\circ}_{\text{glycerol}}\ (\mathrm{V}\ vs.\ \mathrm{RHE}) = E_{\mathrm{SHE}} + \frac{RT}{F} \times ln(10) \times \mathrm{pH}$$

$$= -0.0246\,V + \frac{8.314\ \mathrm{J\ K^{-1}\ mol^{-1}} \times 296.15\ \mathrm{K}}{96485.3321\ \mathrm{C\ mol^{-1}}} \times \ln(10) \times 6.8$$

$$= 0.37\,V$$

Mass activity. Mass activity for the formation of *i* (e.g., glycerol, ethanol, acetate, etc.) was calculated as follows[13]:

$$\text{Mass Activity} = \frac{j_{\text{total}} \cdot FE_i}{\beta \cdot m_{\text{catalyst}}}$$

where j_{total} is the steady-state current density measured under chronoamperometry, FE_i is the Faradaic efficiency to produce the target product i, β is the weight ratio of Cu in the total carbon-supported Cu catalyst, and m_{catalyst} is the catalyst mass.

Turnover frequency (TOF). TOF is expressed in units of $\mu\text{mol s}^{-1}\text{ cm}^{-2}_{\text{catalyst}}$, and $\text{g}_{\text{glycerol}}\text{ h}^{-1}\text{ g}^{-1}_{\text{Cu}}$. TOF for CO_2RR on carbon-supported Cu catalysts was calculated under the assumption that all Cu atoms are atomically dispersed on the carbon surface. For a given product i, TOF is defined as follows[14]:

$$\text{TOF}_i = \frac{\text{Turnover number for } i \text{ formation/geometric area}}{\text{Number of active sites/geometric area}}$$

Turnover number (TON) towards a target product i formation:

$$\text{TON}_i = \left(\frac{j \cdot t \cdot FE_i}{e_i^- \cdot F}\right) \cdot N_A$$

with j being the current density, t the electrolysis time, FE_i the Faradaic efficiency for the formation of a target product i, e_i^- the number of electrons transferred for the formation of one molecule of i, F the Faraday constant ($96485.3321\text{ C mol}^{-1}$), and N_A Avogadro's constant (6.022×10^{23}).

Number of active sites per cm^2 (N):

$$N = \frac{\text{Weight of Cu on electrode}}{M_{\text{Cu}}} \cdot N_A$$

where $M_{\text{Cu}} = 63.546\text{ g mol}^{-1}$ is the molecular mass of Cu.

Alternative expressions for TOF include:

$$\text{TOF}_i\ (\mu\text{mol s}^{-1}\text{ cm}^{-2}_{\text{catalyst}}) = \frac{\text{TON}_i}{N_A}$$

$$\text{TOF}_i\ (\text{g}_{\text{glycerol}}\text{ h}^{-1}\text{ g}^{-1}_{\text{Cu}}) = \frac{\text{TON}_i}{N_A} \cdot \frac{M_i}{\text{weight of Cu on electrode}}$$

where M_i is the molecular mass for the formation of a target product i.

Pearson correlation analysis. Pearson correlation coefficients (r_{XY}) were calculated to assess the linear dependence between pairs of variables, including Cu loading, V_{micro}, V_{meso}, S_{pores}, ECSA, FE of glycerol, n-propanol, ethanol, acetate, acetone, and formate, and the total current density (j_{total}). The coefficient r_{XY} between two variables X and Y was computed using the standard Pearson definition[15,16]:

$$r_{XY} = \frac{\sum_{i=1}^{n} (X_i - \bar{X})(Y_i - \bar{Y})}{\sqrt{\sum_{i=1}^{n} (X_i - \bar{X})^2 \sum_{i=1}^{n} (Y_i - \bar{Y})^2}}$$

where X_i and Y_i are the i-th values in the dataset, and $\bar{X}$ and $\bar{Y}$ are their respective means. Values of r_{XY} range from −1 (perfect negative linear correlation) to +1 (perfect positive linear correlation), with 0 indicating no linear correlation.

4. Advanced Machine Learning

Dataset preparation. The experimental dataset contained data from 104 individual experiments. For each experiment, the applied potential, copper loading, type of carbon support, and faradaic efficiencies of chemical species were recorded and inserted into the dataset as an individual datapoint. The type of carbon support was described by three parameters-average pore area, ratio of microporous volume to the total volume, and ratio of mesoporous volume to the total volume. The faradaic efficiencies of chemical species were regarded as the targets while the applied potential, copper loading, and the three parameters describing the type of carbon support were used as the features for training predictive models.

Predictive model. Predictive models for simultaneous prediction of the faradaic efficiencies of the chemical species based on the experimental conditions were developed by employing the Extreme Gradient Boosting regression algorithm (`XGBRegressor`) using the XGBoost library in Python[17]. XGBoost is a highly efficient and optimized library used for gradient boosting applications, which implements a recursive binary splitting strategy to identify the optimal split at each iteration, enhancing the model's predictive performance. The tree-based framework of the algorithm renders it insensitive to outliers, and like other boosting methods, it exhibits robustness against overfitting, which greatly simplifies the model selection process. Additionally, XGBoost has been successfully used in many scientific fields and has been used extensively by the machine learning community to develop award-winning data science solutions[18]. Since the task here involved multi-target regression, a number of XGBRegressor models were trained, with a separate model per each target variable, by utilizing the `MultiOutputRegressor` class in the Scikit-learn library for simultaneous prediction of all targets[19]. XGBRegressor excels at learning nonlinear patterns and interactions in data. Each regression tree in XGBoost splits data based on feature thresholds, effectively modeling piecewise relationships. This means XGBRegressor can fit complex curves or threshold effects that Pearson correlation would overlook. In fact, boosted decision trees capture complex, non-linear patterns in data far better than linear models. Additionally, XGBRegressor naturally accounts for feature interactions: if catalyst support type, an XGBoost tree can first split by support type (C_{micro} vs. C_{meso}, for example) and then learn different pore size–performance relationships in each subgroup. This way, XGBRegressor develops a predictive model that mirrors true multivariate relationships, whereas correlation analysis remains blind to anything beyond one-to-one linear links. As a result, XGBRegressor improves prediction accuracy for CO_2RR performance because it is not restricted to straight-line trends like Pearson correlation.

AI/ML method is applied to conclude the relevance of the factors (pore structure, products, etc.). The learning curve of predictive models trained with increasing data shows that, with less than 25% of data, the training score is much higher than the test score. As more data is added, the test score improves, with models nearing optimal performance at 80% of the dataset. Despite the small dataset size (104 datapoints), the XGB regressor achieves an $R^2 > 0.8$, demonstrating strong predictive capability and high feature-target correlation. After validating the regressive models' usability, final models with optimized hyperparameters were trained on 80% of the dataset. The test performance on the remaining 20% achieved an overall R^2 score of 0.84. Despite the small dataset, the models effectively predict faradaic efficiencies under varying experimental conditions. The prediction model was found to be accurate for FE predication of glycerol, ethanol, formate, etc.

Supplementary Figures

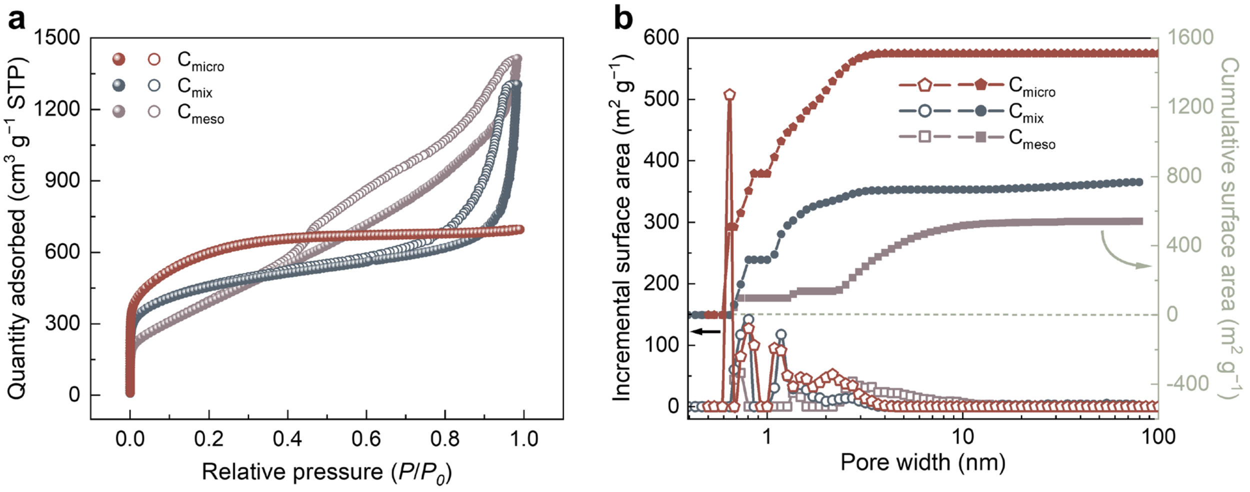

Supplementary Fig. 1 | N_2 adsorption isotherms and correlation of pore distribution and SSA with C_{micro}, C_{mix}, and C_{meso}. a. N_2 adsorption (solid circles) and desorption (hollow circles) isotherms of C_{micro}, C_{mix}, and C_{meso} measured at 77 K. An almost ideal Type I isotherm was exhibited by the C_{micro}. A typical type IVa isotherm was exhibited by C_{meso}. A composite isotherm encompassing both Type I and Type IVa is observed for C_{mix}. They all have SSAs higher than 1000 m^2 g^{-1} with C_{micro} being the highest. **b.** Incremental surface area (hollow symbols) and cumulative surface area (solid symbols) of C_{micro}, C_{mix}, and C_{meso} are plotted as functions of the pore width distribution in the 100 nm range. These values were calculated from the adsorption branch of the isotherm using N_2 at 77 K. Compared to larger pores, micropores of equivalent volume are observed to contribute more significantly to the BET specific surface area.

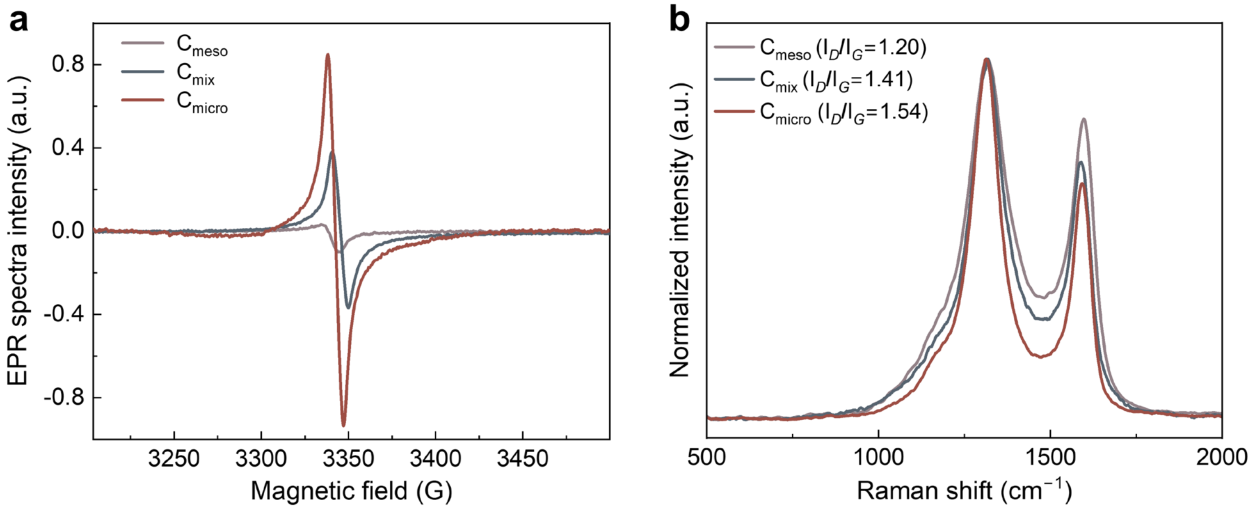

Supplementary Fig. 2 | EPR and Raman spectroscopy of C_{micro}, C_{mix}, and C_{meso}. a. EPR spectra of C_{micro}, C_{mix}, and C_{meso} show that C_{micro} has the strongest signal among the three, indicating that it has the highest concentration of paramagnetic centers from the unpaired electrons due to surface defects. The greater the number of defects in the carbon structure, the more unpaired electrons are present. Consequently, the intensity of the EPR signal increases with the quantity of defects, as the signal is directly proportional to the concentration of paramagnetic centers (unpaired electrons) in the sample; **b.** Raman spectra of C_{micro}, C_{mix}, and C_{meso} identify that C_{micro} has the highest D-band to G-band ratio therefore the lowest degree of graphitization.

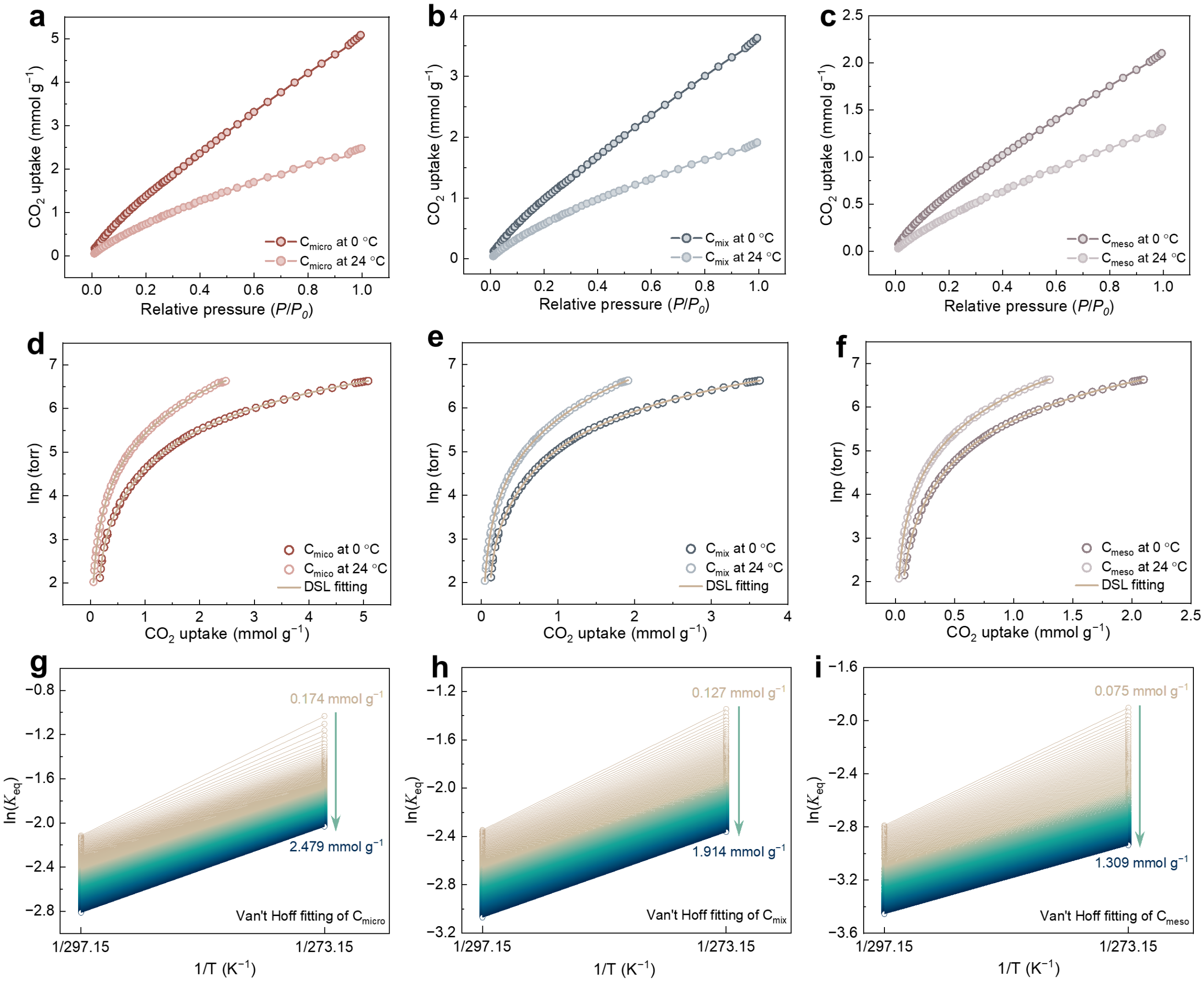

Supplementary Fig. 3 | CO_2 adsorption isotherms, dual-site Langmuir (DSL) fitting, and van't Hoff plot at 0 °C and 24 °C. **a-c.** CO_2 adsorption isotherms on C_{micro}, C_{mix} and C_{meso} at 0°C and 24°C. **d-f,** DSL fitting for CO_2 adsorption isotherms of C_{micro}, C_{mix} and C_{meso} at 0°C and 24°C was performed, and from these analyses, were used to derive the corresponding enthalpy of CO_2 adsorption. **g-i.** The van't Hoff plots for C_{micro}, C_{mix}, and C_{meso}. The slope and intercept of the resulting line can be directly used to calculate $-\Delta H_{ads}$ and $-\Delta S_{ads}$: $-\Delta H_{ads} = R \times \text{slope}$; $-\Delta S_{ads} = -R \times \text{intercept}$.

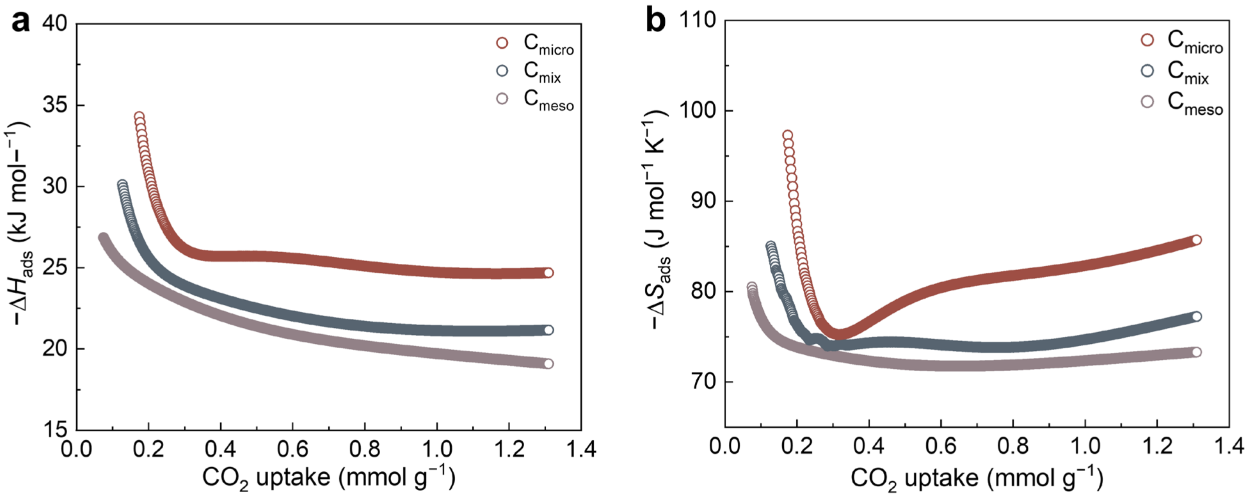

Supplementary Fig. 4 | Enthalpy and entropy of CO_2 adsorption. Enthalpy (**a**) and entropy (**b**) of CO_2 adsorption on C_{micro}, C_{mix}, and C_{meso}. The $-\Delta H_{ads}$ and $-\Delta S_{ads}$ for C_{micro} and C_{mix} significantly dropped near a coverage of half, affirming the occupation of adsorption sites in the material. The gradual rise in $-\Delta H_{ads}$ and $-\Delta S_{ads}$ can be attributed to the increased intermolecular interactions between the adsorbed CO_2 molecules as the CO_2 coverage, causing increased van der Waals forces or even the formation of some ordered structures. These effects are most pronounced for C_{micro} as the result of stronger nanoconfinement.

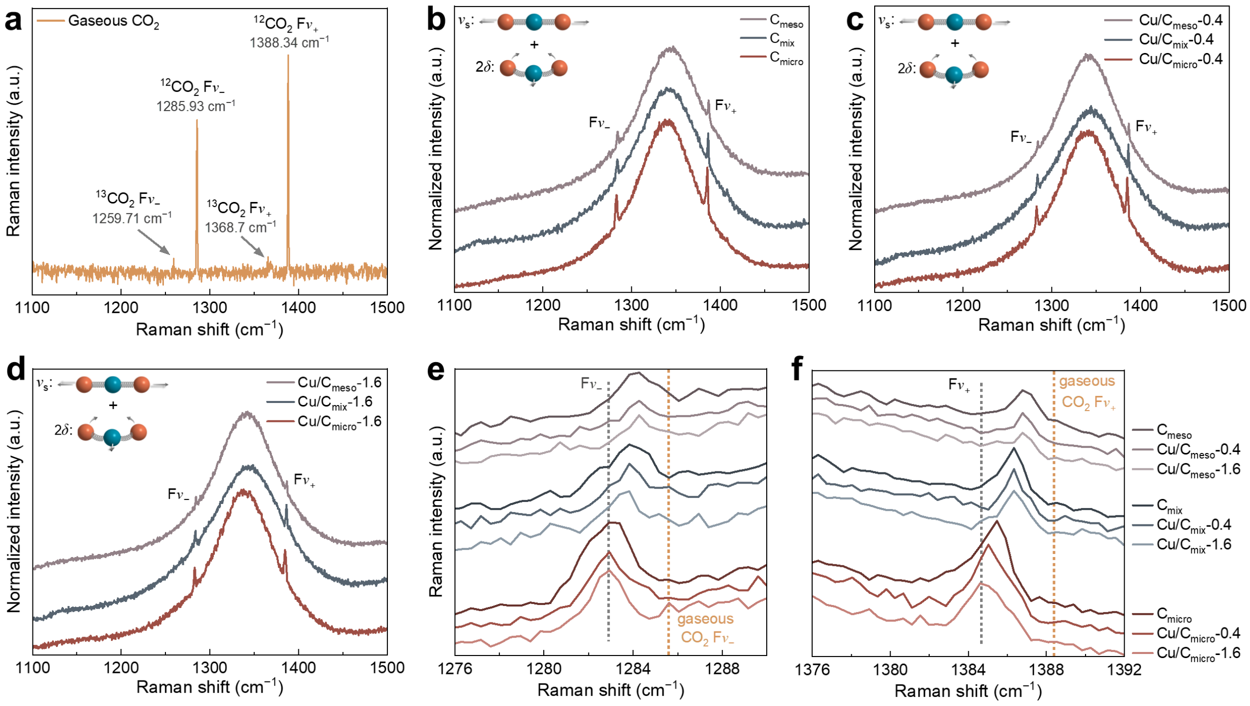

Supplementary Fig. 5 | Raman spectroscopy of CO_2 adsorption. a. Raman spectroscopy of gaseous CO_2. Raman spectroscopy of gaseous CO_2 reveals two principal vibrational peaks, located at 1285.93 cm^{-1} and 1388.34 cm^{-1}, respectively. These two peaks, known as the Fermi diad, arise from Fermi resonance coupling between two vibrational modes of the CO_2 molecule[20]. The peak at 1388.34 cm^{-1} corresponds to the fundamental frequency of symmetric stretching vibrations (ν_s) of CO_2. In this vibrational mode, the two C=O bonds in the linear CO_2 molecule stretch in a symmetric manner simultaneously. The peak at 1285.93 cm^{-1} corresponds to the first overtone of bending vibrations of CO_2 (twice the frequency of the bending mode δ, denoted as 2δ). CO_2 possesses two degenerate bending vibrational modes (δ, approximately 667 cm^{-1}), and when two quanta of bending vibration are excited, their energy approaches that of the ν_s mode. Due to this accidental degeneracy, the symmetric ν_s and the overtone of 2δ strongly couple, leading to Fermi resonance, which results in the splitting of the original single energy level into two mixed states[21]. The high-frequency peak at 1388 cm^{-1} is primarily characterized by symmetric stretching (Fν_+), whereas the low-frequency peak at 1286 cm^{-1} predominantly features bending vibrations (Fν_-). However, both peaks result from a mixture of these two vibrational modes: ν_s and 2δ. **b.** Raman spectroscopy of CO_2 adsorbed on C_{micro}, C_{mix}, and C_{meso}, respectively. **c.** Raman spectroscopy of CO_2 adsorbed on Cu/C_{micro}-0.4, Cu/C_{mix}-0.4, and C_{meso}-0.4, respectively. **d.** Raman spectroscopy of CO_2 adsorbed on Cu/C_{micro}-1.6, Cu/C_{mix}-1.6, and C_{meso}-1.6, respectively. **e.** In the Raman spectra, the Fν_- peaks were observed for CO_2 adsorbed on C_{micro}, C_{mix}, and C_{meso}, as well as after loading with 0.4 wt.% and 1.6 wt.% Cu, respectively. **f.** In the Raman spectra, the Fν_+ peaks were observed for CO_2 adsorbed on C_{micro}, C_{mix}, and C_{meso}, as well as after loading with 0.4 wt.% and 1.6 wt.% Cu, respectively. After adsorption of CO_2 on C_{micro}, C_{mix}, and C_{meso}, the Raman vibrational peaks (Fν_+ and Fν_-) exhibit a red shift compared to gaseous CO_2. This red shift arises from the decreased vibrational frequencies due to the interactions between the CO_2 molecules and the pore surfaces. Fundamentally, these interactions weaken the effective force constants within the CO_2 molecules, thereby lowering the vibrational energy and reducing the vibrational frequencies. The extent of the red shift varies across different pore structures in carbon materials due to the differing strengths of interaction with CO_2. For C_{micro}, the narrow micropores strongly physically adsorb the CO_2 molecules entering them. On one hand, the van der Waals and electrostatic interactions between quadrupole moment of CO_2 and the surface electric fields of the micropore walls are compounded within the confined space, resulting in stronger overall attraction. On the other hand, the restricted space in micropores tightly "fixes" the CO_2 near the pore walls, leading to polarization or slight distortion of the C=O bonds and a consequent notable reduction in vibrational frequency. For C_{meso}, due to its larger mesopore size, the surface attraction exerted on CO_2 is relatively dispersed and weaker than in micropores. The interaction mainly occurs when the molecule approaches the pore walls, and the larger pore size means that the forces cannot act on the molecule from multiple directions as in micropores. Thus, the CO_2 is less tightly bound in mesopores, causing minimal disturbance to the molecular structure and correspondingly, a very slight red shift in the Raman peaks. For C_{mix}, which features both micro and mesopore structures, the interactions with CO_2 lie between those observed in C_{micro} and C_{meso}. Some of the CO_2 might be adsorbed in the micropores (leading to a larger red shift), while some might adhere to the mesopores or surface areas (resulting in a smaller red shift). Consequently, the overall Raman spectra exhibit a moderate red shift, less than that seen with C_{micro} but more significant than that of C_{meso}. Adsorption thermodynamics parameters further corroborate these conclusions, with CO_2 adsorption on C_{micro} displaying the highest $-\Delta H_{ads}$ and $-\Delta S_{ads}$. A larger exothermic value (more negative ΔH_{ads}) indicates stronger interactions or deeper adsorption wells between CO_2 and the micropore surfaces, consistent with the observed peak red shift: stronger interactions lead to significantly lower vibrational frequencies. Moreover, the confinement of CO_2 from a gaseous free state to a restricted micropore results in a substantial decrease in entropy (higher $-\Delta S_{ads}$), indicating that the molecules are highly orderly bound within the pores. The high $-\Delta H_{ads}$ and $-\Delta S_{ads}$ values reflect the strongest binding of CO_2 in micropores, hence the largest red shift in their Raman peaks, adhering to the principle that stronger adsorption leads to greater frequency reduction. CO_2 adsorption on C_{meso} shows the smallest $-\Delta H_{ads}$ and a lesser $-\Delta S_{ads}$. Due to the shallower adsorption potential provided by mesopores, the interaction between CO_2 and the surface is weaker, resulting in less heat released during the adsorption process. Also, the spacious mesopore allows for some degree of freedom for the molecules, resulting in a smaller entropy loss compared to micropores. The lower $-\Delta H_{ads}$ and the smaller decrease in ΔS_{ads} signify only weak binding of CO_2, corresponding to a lesser reduction in the vibrational frequency. Thus, the smallest red shift in the Raman peaks is observed on C_{meso}. C_{mix} exhibits $-\Delta H_{ads}$ and $-\Delta S_{ads}$ values that lie between the aforementioned extremes. The presence of both strong binding sites provided by micropores and weaker binding regions from meso/large pores leads to an intermediate overall adsorption heat effect and entropy change, with CO_2 being partly strongly bound and partly freer. This is reflected in the Raman spectrum as a moderate degree of peak red shift, more significant than on C_{meso} but weaker than on C_{micro}. After loading 0.4 wt.% and 1.6 wt.% Cu on C_{mix} and C_{meso}, there were no further changes observed in the Raman spectra of CO_2 for the $F\nu_+$ and $F\nu_-$ peaks. However, further changes in the adsorption and vibrational behavior of CO_2 were noted upon Cu loading on C_{micro}. Raman spectroscopy revealed that as the Cu loading increased, a more pronounced redshift occurred in the $F\nu_+$ peak of the CO_2 Raman spectrum. Our interpretation is that the single-atom Cu serves as a Lewis acid site, coordinating with the O atoms (Lewis base sites) in the CO_2 molecule. This interaction leads to a significant deviation of the CO_2 molecule from its linear symmetric structure, such as bending at a certain angle or altering bond lengths, while simultaneously weakening the C=O bond strength. This results in a notable decrease in the frequency of the $F\nu_+$, manifesting as a greater redshift in the Raman spectrum. With an increase in Cu content, more active sites are available for coordination, affecting more CO_2 molecules intensely, thereby making the overall peak shift more pronounced.

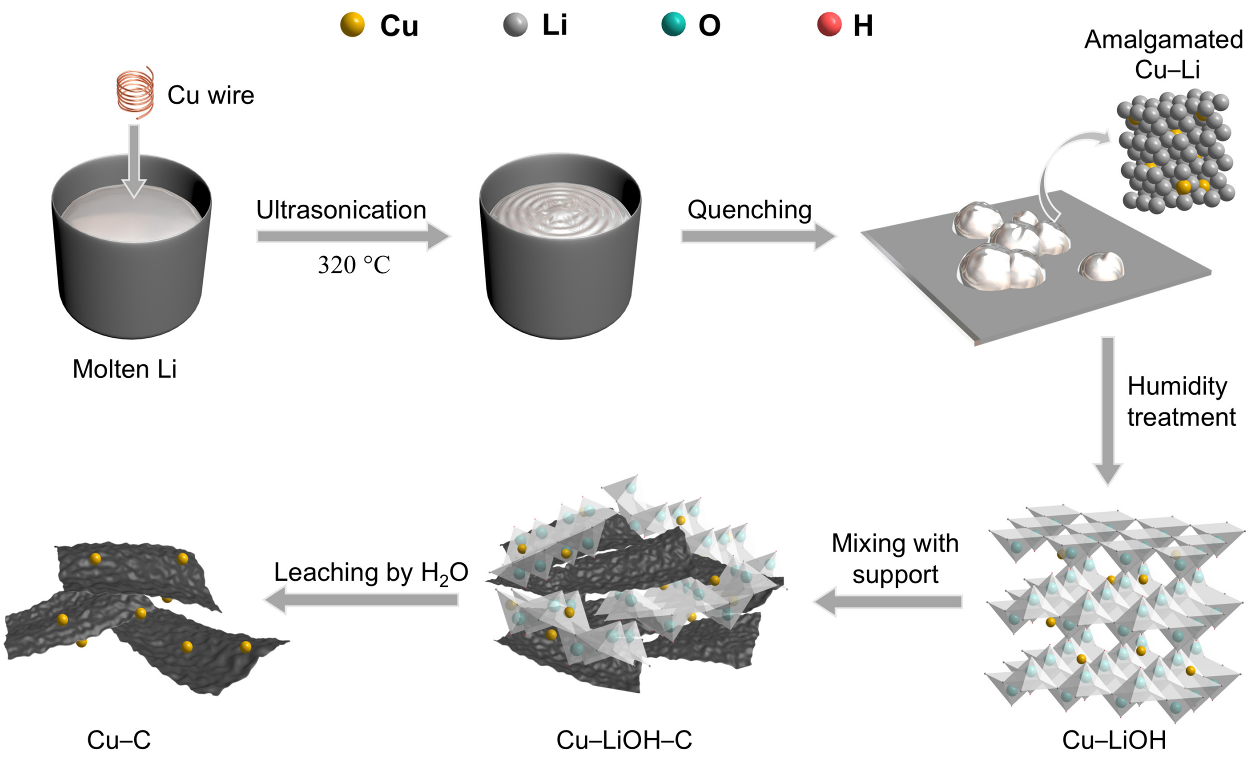

Supplementary Fig. 6 | Catalyst synthesis. The carbon-supported Cu SA catalyst was prepared using a sequential procedure that employed the amalgamated Cu–Li method. Wire Cu is introduced into molten Li and subjected to sonication until complete dissolution is achieved. Subsequently, during the quenching of the lithium melt to room temperature, Cu remains in an atomically isolated state. The Li is then converted to LiOH under humidified air, resulting in the formation of a Cu–LiOH mixture. This mixture is blended with carbon support (C_{micro}, C_{mix}, or C_{meso}, and subsequent removal of LiOH is carried out through water leaching. As a result, the Cu atoms are transferred onto the carbon surface. Notably, due to the ambient temperature conditions in the transfer process, Cu atom migration and agglomeration are effectively minimized, allowing them to predominantly maintain an atomically dispersed form.

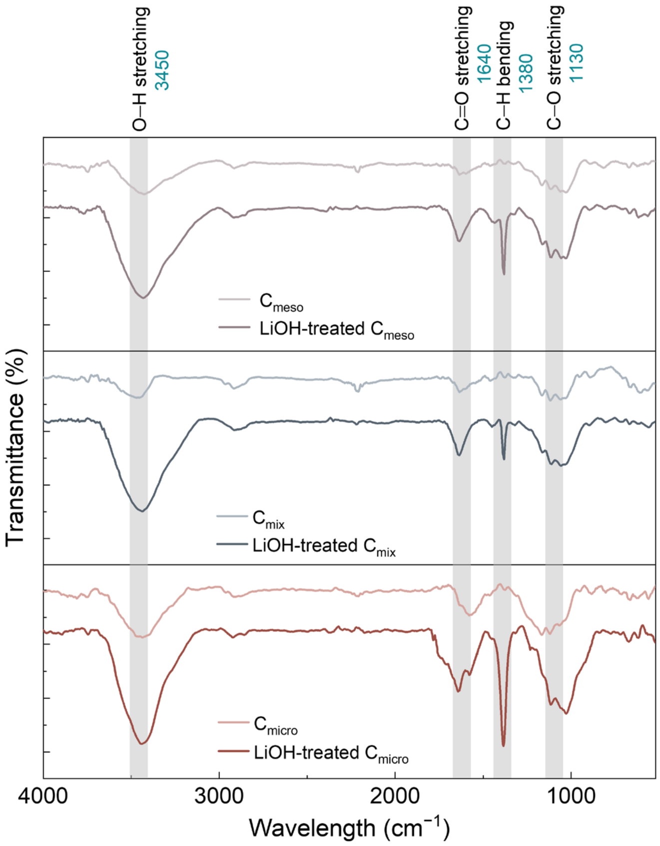

Supplementary Fig. 7 | Fourier-transform infrared spectroscopy (FT-IR). The FT-IR spectra of the untreated carbons and those treated with LiOH were carried out to simulate the strong alkaline environment during water leaching step to remove lithium hydroxide from metal-LiOH-carbon mixture in the ALM synthesis. It was observed that the LiOH-treated carbons exhibited enhanced intensities of functional groups in comparison to the untreated carbons. Specifically, a distinct peak within the wavelength range of 3000–3650 cm^{-1} was observed, displaying a wide and broad transmission band with its maximum intensity at 3450 cm^{-1}. This characteristic transmission band was attributed to the stretching mode of the O–H bonds present in hydrogen-bonded hydroxyl groups attached to the carbon structure, produced by treatment of highly caustic LiOH solution. At 1640 cm^{-1}, another peak was detected, which was ascribed to the stretching vibrations of C=O bonds in the conjugated hydrocarbon. Importantly, this signal exhibited a weaker intensity in the untreated carbons. Moreover, the LiOH treatment resulted in an increased intensity of the C–H aliphatic bending vibrations at 1380 cm^{-1}. Additionally, the presence of a broad transmission band enhancement at approximately 1130 cm^{-1} provided evidence for the stretching vibrations of the C–O bonds.

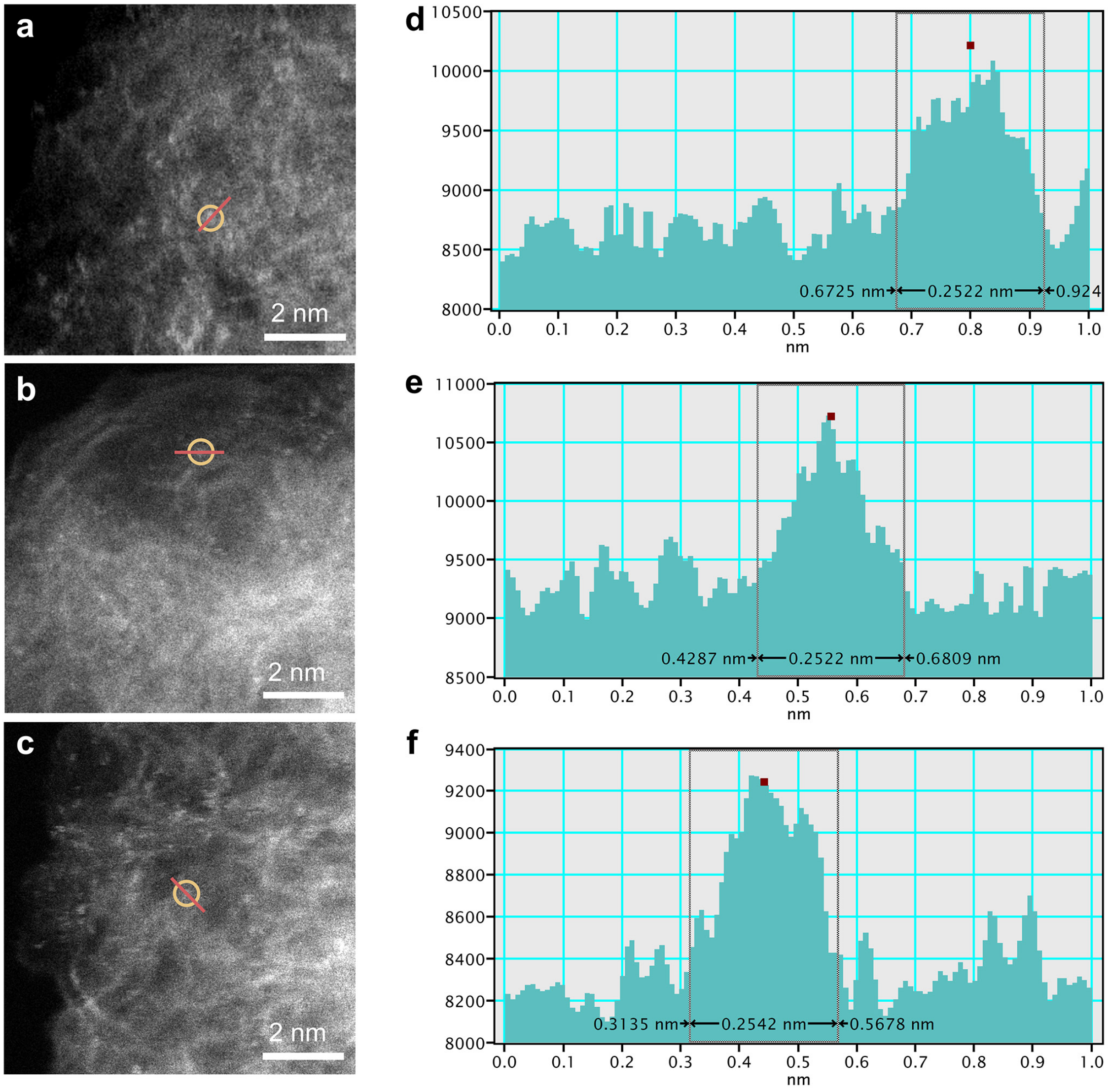

Supplementary Fig. 8 | High-magnification HAADF-STEM imaging analysis of Cu/C$_{\text{micro}}$-0.4, Cu/C$_{\text{mix}}$-0.4, and Cu/C$_{\text{meso}}$-0.4. a-c. Representative high-magnification HAADF–STEM images of Cu single atoms in Cu/C$_{\text{micro}}$-0.4, Cu/C$_{\text{mix}}$-0.4 and Cu/C$_{\text{meso}}$-0.4, respectively. Intensity profile of **d.** Cu/C$_{\text{micro}}$-0.4, **e.** Cu/C$_{\text{mix}}$-0.4 and **f.** Cu/C$_{\text{meso}}$-0.4 single atomic column along the white line in **a-c**. The intensity distributions show the peaks at Cu/C$_{\text{micro}}$-0.4, Cu/C$_{\text{mix}}$-0.4, and Cu/C$_{\text{meso}}$-0.4 with full widths at half maximum of approximately 2.522 Å, 2.522 Å, and 2.542 Å, respectively. These values closely align with the Cu atomic diameter of 2.56 Å.

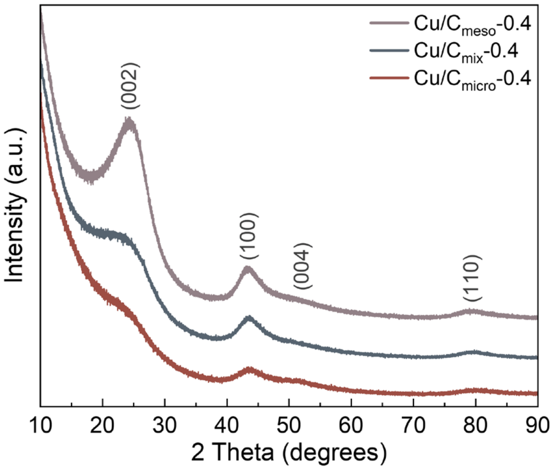

Supplementary Fig. 9 | PXRD spectra of Cu/C$_{micro}$-0.4, Cu/C$_{mix}$-0.4, and Cu/C$_{meso}$-0.4. In the PXRD patterns, the variations in peak intensities and positions for the (002), (100), (004), and (110) planes among the 3 catalysts suggest differences in the structural properties of the carbon supports**.** The Cu/C$_{meso}$-0.4 sample exhibits the most pronounced (002) and (110) peaks, indicative of the highest degree of graphitization and the most well-ordered interlayer structure. Notably, there is an absence of distinct peaks attributable to Cu, suggesting that the Cu atoms are highly dispersed on the carbon substrates, and have not formed any long-range ordered structures.

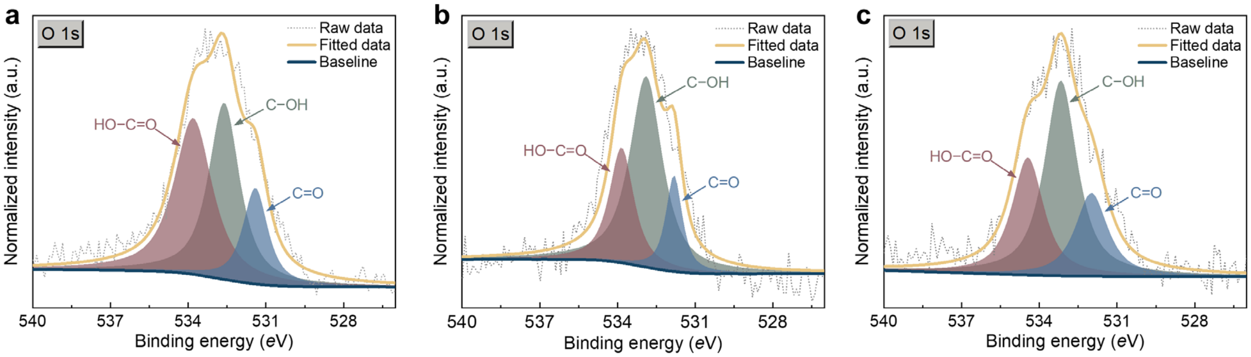

Supplementary Fig. 10 | XPS spectra of O 1s of Cu/C$_{micro}$-0.4, Cu/C$_{mix}$-0.4, and Cu/Cmeso-0.4. The O-containing functional groups on the surfaces of the catalysts **a.** Cu/C$_{micro}$-0.4, **b.** Cu/C$_{mix}$-0.4, and **c.** Cu/C$_{meso}$-0.4 are similar, comprising hydroxyl groups (–OH), carbonyl groups (C=O), and carboxyl groups (–COOH).

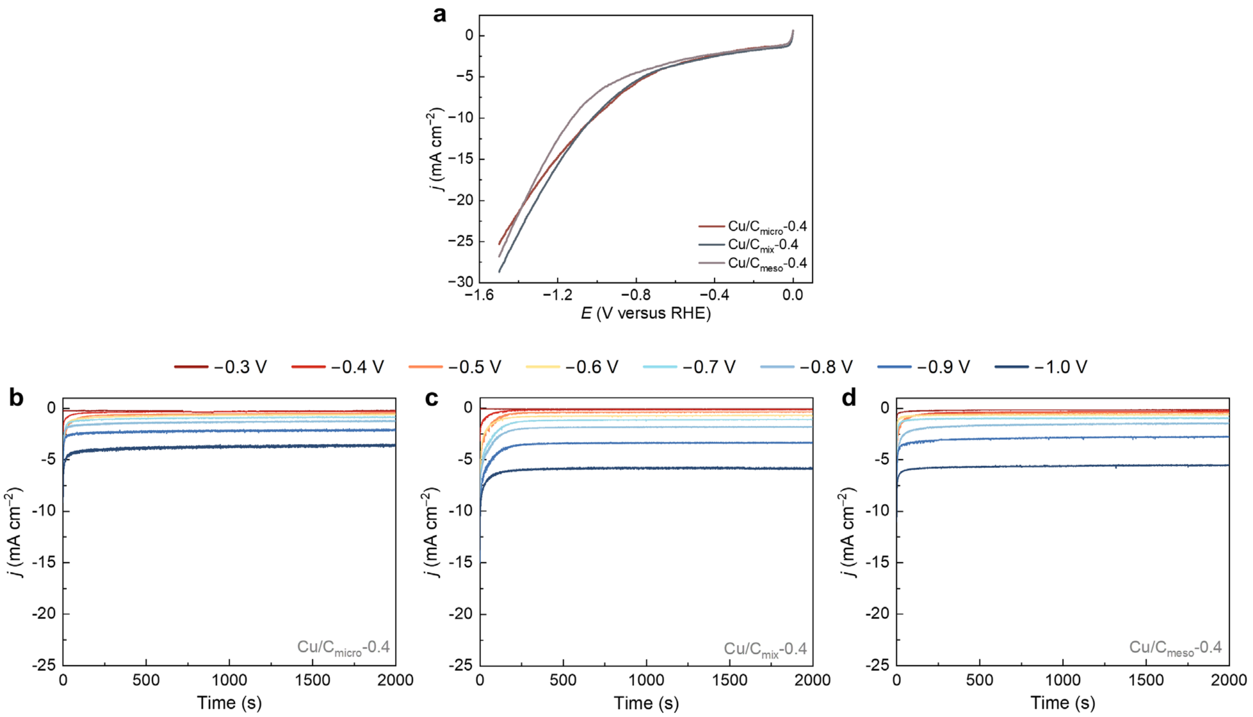

Supplementary Fig. 11 | LSV and chronoamperometry of $\mathrm{Cu/C_{micro}}$-0.4, $\mathrm{Cu/C_{mix}}$-0.4, and $\mathrm{Cu/C_{meso}}$-0.4. a. LSVs of $\mathrm{Cu/C_{micro}}$-0.4, $\mathrm{Cu/C_{mix}}$-0.4, and $\mathrm{Cu/C_{meso}}$-0.4 in CO_2-saturated 0.1 M $KHCO_3$ from 0 to −1.5 V (scan rate: 2 mV s^{-1}). **b-d.** The current density as the function of time for $\mathrm{Cu/C_{micro}}$-0.4, $\mathrm{Cu/C_{mix}}$-0.4, and $\mathrm{Cu/C_{meso}}$-0.4 measured at different potentials during the chronoamperometry experiments.

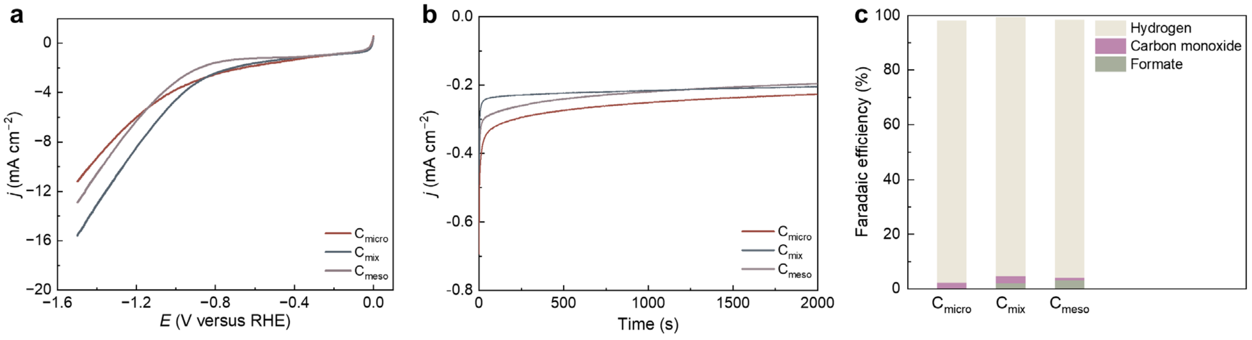

Supplementary Fig. 12 | CO_2RR on bare of carbon support. a. LSVs (scan rate: 10 mV s^{-1}) over the amorphous carbons treated by the same ALM "catalyzing" process without Cu added in the molten Li. **b.** The current densities as the function of time measured at −0.7 V cell potentials. **c.** The corresponding FEs observed at 3 different cell potentials with H_2 being the sole or dominant products.

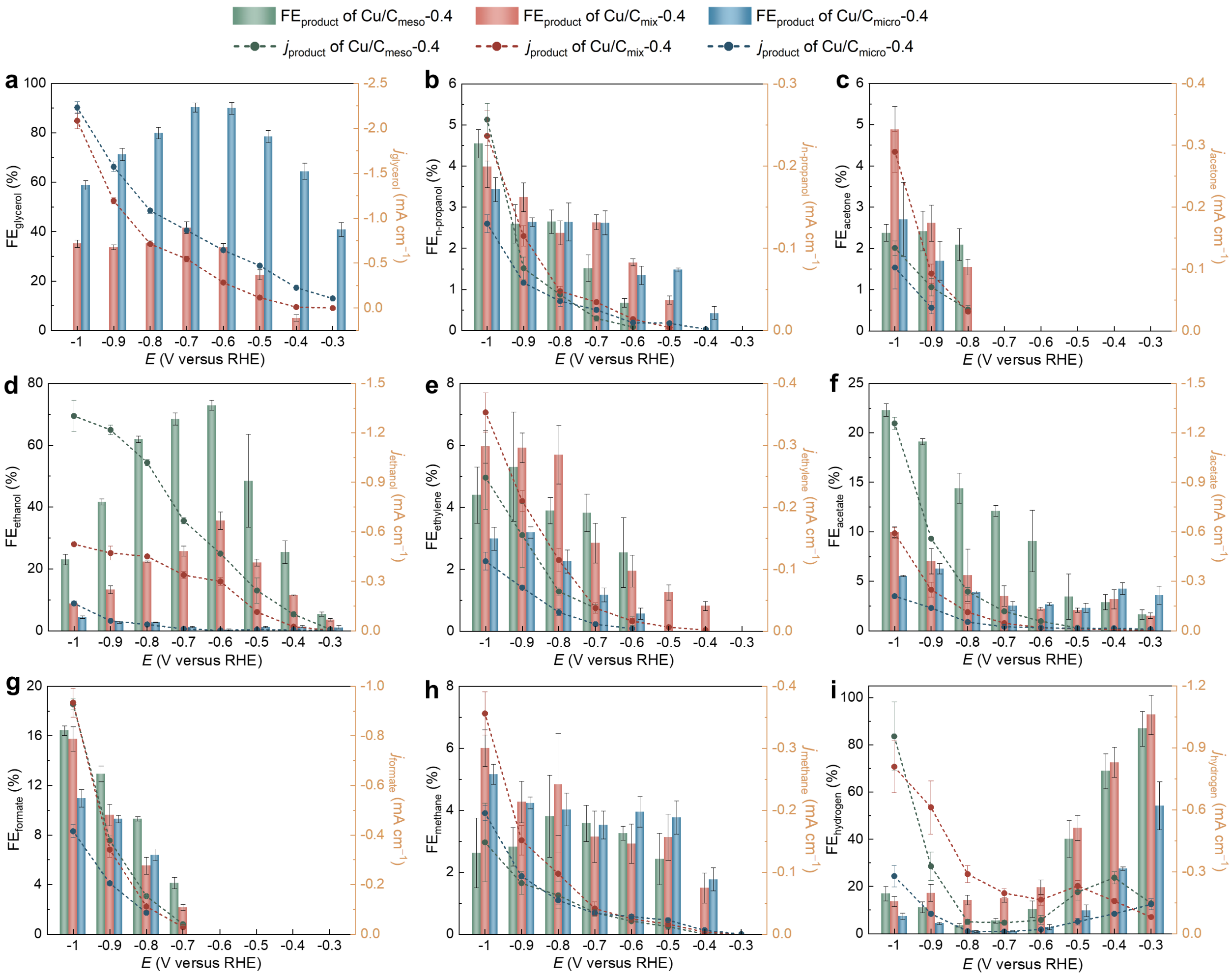

Supplementary Fig. 13 | Complete analyses of partial FEs and partial j for specific products from Cu/C$_{micro}$-0.4, Cu/C$_{mix}$-0.4, and Cu/C$_{meso}$-0.4. The FEs for CO2RR (left y-axes) and the partial $j_{product}$ of the products (right Y-axes) for Cu/C$_{micro}$-0.4, Cu/C$_{mix}$-0.4, and Cu/C$_{meso}$-0.4. **a.** glycerol. **b.** n-propanol. **c.** acetone. **d.** ethanol. **e.** ethylene. **f.** acetate. **g.** formate. **h.** methane. **i.** hydrogen.

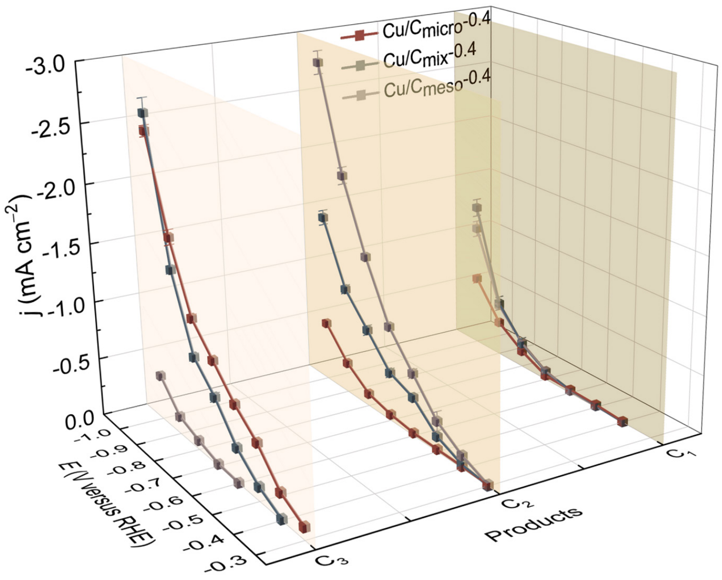

Supplementary Fig. 14 | Comparative analysis of current densities *j* for CO_2-to-C_3, C_2, and C_1 from Cu/C_{micro}-0.4, Cu/C_{mix}-0.4, and Cu/C_{meso}-0.4 at different potentials.

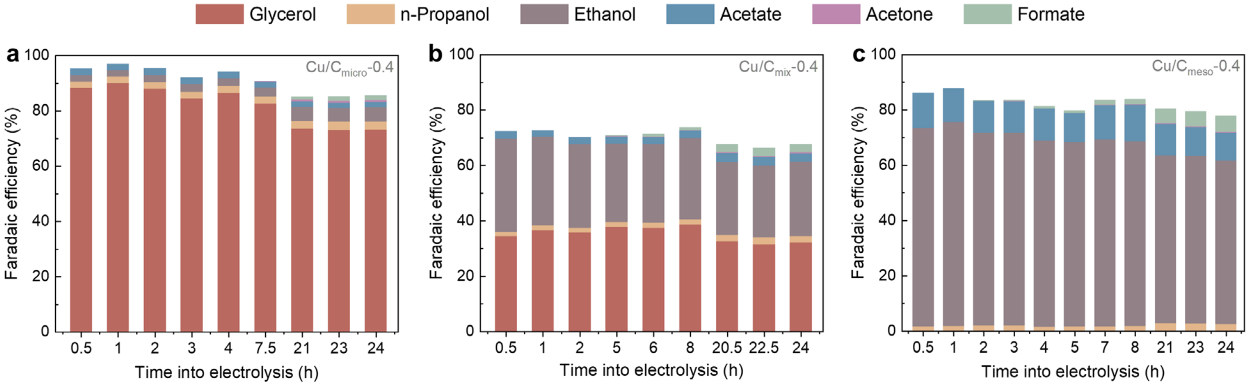

Supplementary Fig. 15 | Distribution of products from long-term electrolysis of **a.** Cu/C_{micro}-0.4, **b.** Cu/C_{mix}-0.4, and **c.** Cu/C_{meso}-0.4 at −0.7 V varies over time.

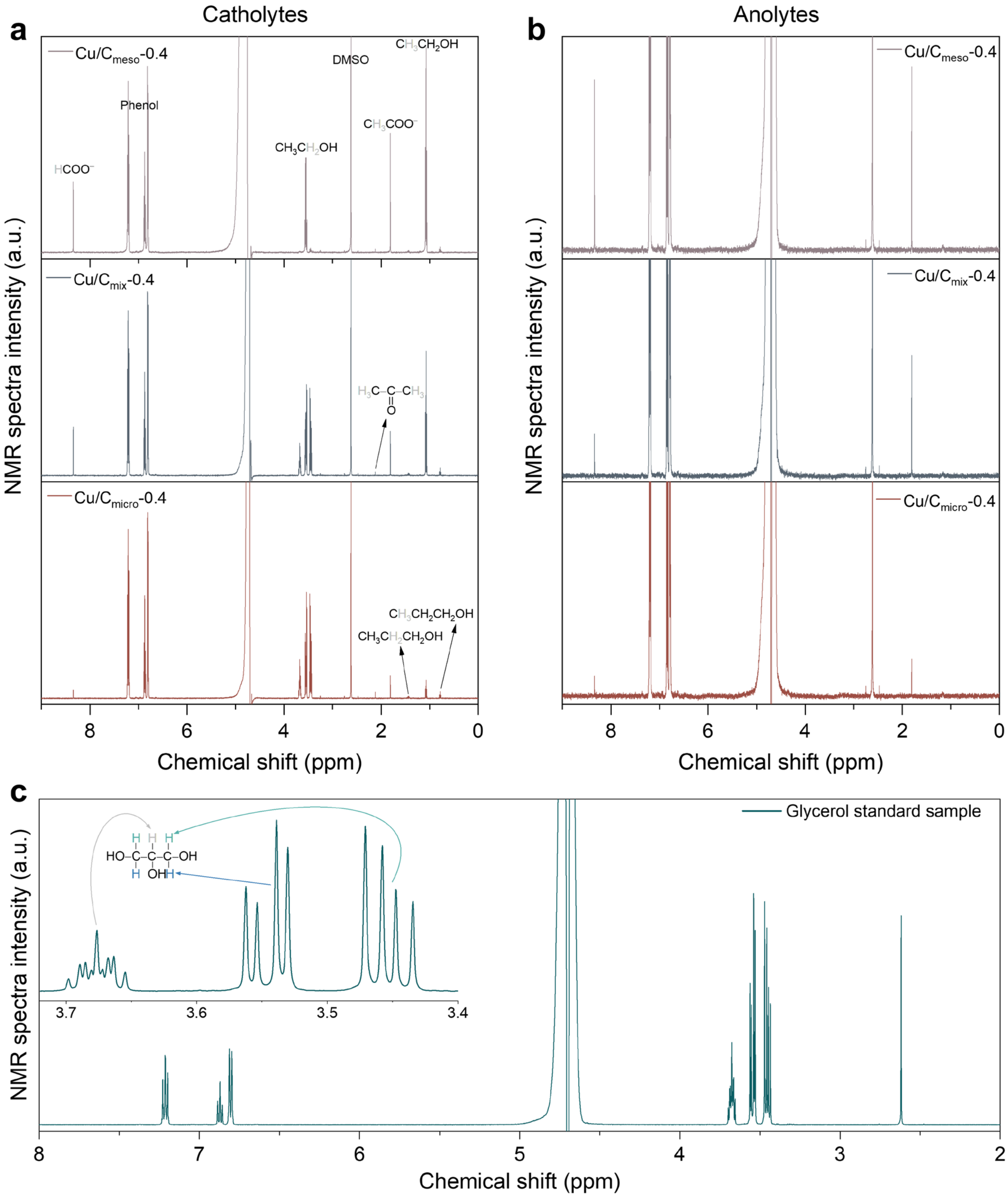

Supplementary Fig. 16 | Representative liquid products analysis. NMR spectra of the **a.** catholyte, **b.** anolyte taken after long-term electrocatalysis over Cu/C$_{micro}$-0.4, Cu/C$_{mix}$-0.4, and Cu/C$_{meso}$-0.4 at -0.7 V (versus RHE). **c.** from 5 mM standard glycerol sample in 0.1 M $KHCO_3$ solution with DMSO and phenol as internal standard in D_2O; The inset is the magnified part of one nonet and two quartets peak of glycerol, each attributed to protons in different chemical environments. The origin of each peak is indicated by protons depicted in distinct colors.

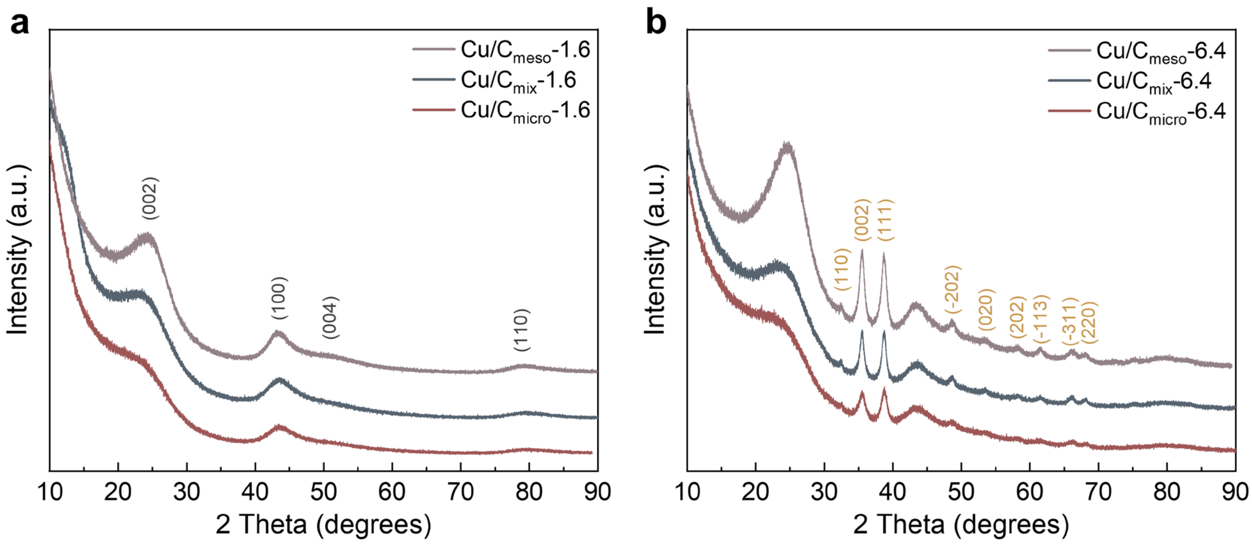

Supplementary Fig. 17 | XRD spectra of Cu/C$_{\mathrm{micro}}$, C$_{\mathrm{mix}}$, C$_{\mathrm{meso}}$-1.6, and Cu/C$_{\mathrm{micro}}$, C$_{\mathrm{mix}}$, C$_{\mathrm{meso}}$-6.4. a. XRD spectra of Cu/C$_{\mathrm{micro}}$-1.6, Cu/C$_{\mathrm{mix}}$-1.6, and Cu/C$_{\mathrm{meso}}$-1.6. **b.** XRD spectra of Cu/C$_{\mathrm{micro}}$-6.4, Cu/C$_{\mathrm{mix}}$-6.4, and Cu/C$_{\mathrm{meso}}$-6.4. When the loading of Cu reached 6.4 wt.%, XRD peaks associated with CuO were observed on all three types of carbon supports, with the full width at half maximum (FWHM) of the CuO (111) diffraction peak ranging from 2θ = 3.52° on Cu/C$_{\mathrm{micro}}$-6.4 to 2θ = 3.043° on Cu/C$_{\mathrm{mix}}$-6.4, and 3.0086 on Cu/C$_{\mathrm{meso}}$-0.4. Using the Scherrer equation[22,23], the crystal size of CuO on the three carbon supports was estimated. The equation $D = \frac{K\lambda}{\beta\cos\,\theta}$, where D is the crystal size in nanometers; K is the shape factor, and its value is 0.9; λ is the wavelength of the X-ray used (Cu K_{α} radiation with 40 mA, 40 kV, $\lambda = 0.15418$ nm); β is the FWHM of the diffraction peak, in radians; θ is the Bragg angle (half the diffraction angle). The calculated sizes of CuO were 2.38 nm on Cu/C$_{\mathrm{micro}}$-6.4, 2.75 nm on Cu/C$_{\mathrm{mix}}$-6.4, and 2.81 nm on Cu/C$_{\mathrm{meso}}$-6.4.

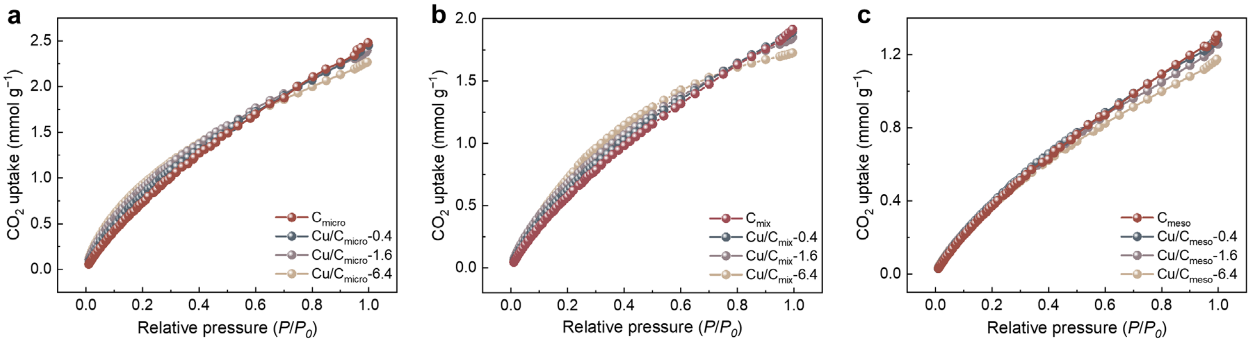

Supplementary Fig. 18 | Changes in CO_2 adsorption isotherms with variations of Cu loading on different carbon supports. CO_2 adsorption isotherms at different Cu loadings of 0 wt. %, 0.4 wt. %, 1.6 wt. % and 6.4 wt. %. on **a.** C_{micro}, **b.** C_{mix} and **c.** C_{meso}. On C_{micro}, an increase in Cu loading correlates with enhanced CO_2 uptake at lower relative pressures in the isotherm. This enhancement can be attributed to the incorporation of Cu atoms into the micropores, leading to a reduction in pore size and enabling rapid CO_2 adsorption at reduced pressures. With further increases in Cu loading, larger Cu grains partially cover the micropore entrances—creating smaller pore spaces without blocking them, which if blocked, would not result in increased CO_2 capture at low pressures. Macroscopically, this phenomenon indicates an increase in CO_2 selectivity on C_{micro} with higher Cu loadings. On C_{meso}, increased Cu loading leads to the filling of mesopores. The incorporation of Cu into these mesopores has a negligible impact, with no observable changes in CO_2 adsorption at low and medium relative pressures. Overall, as Cu loading increases across three carbon supports, CO_2 adsorption on the catalysts enhances microporous behavior, yet the effect on mesoporous behavior is almost negligible. Moreover, with increased Cu loading, the overall adsorption capacity at a relative pressure of 1 decrease across all carbon supports, attributable to the substantially greater mass of Cu atoms compared to carbon.

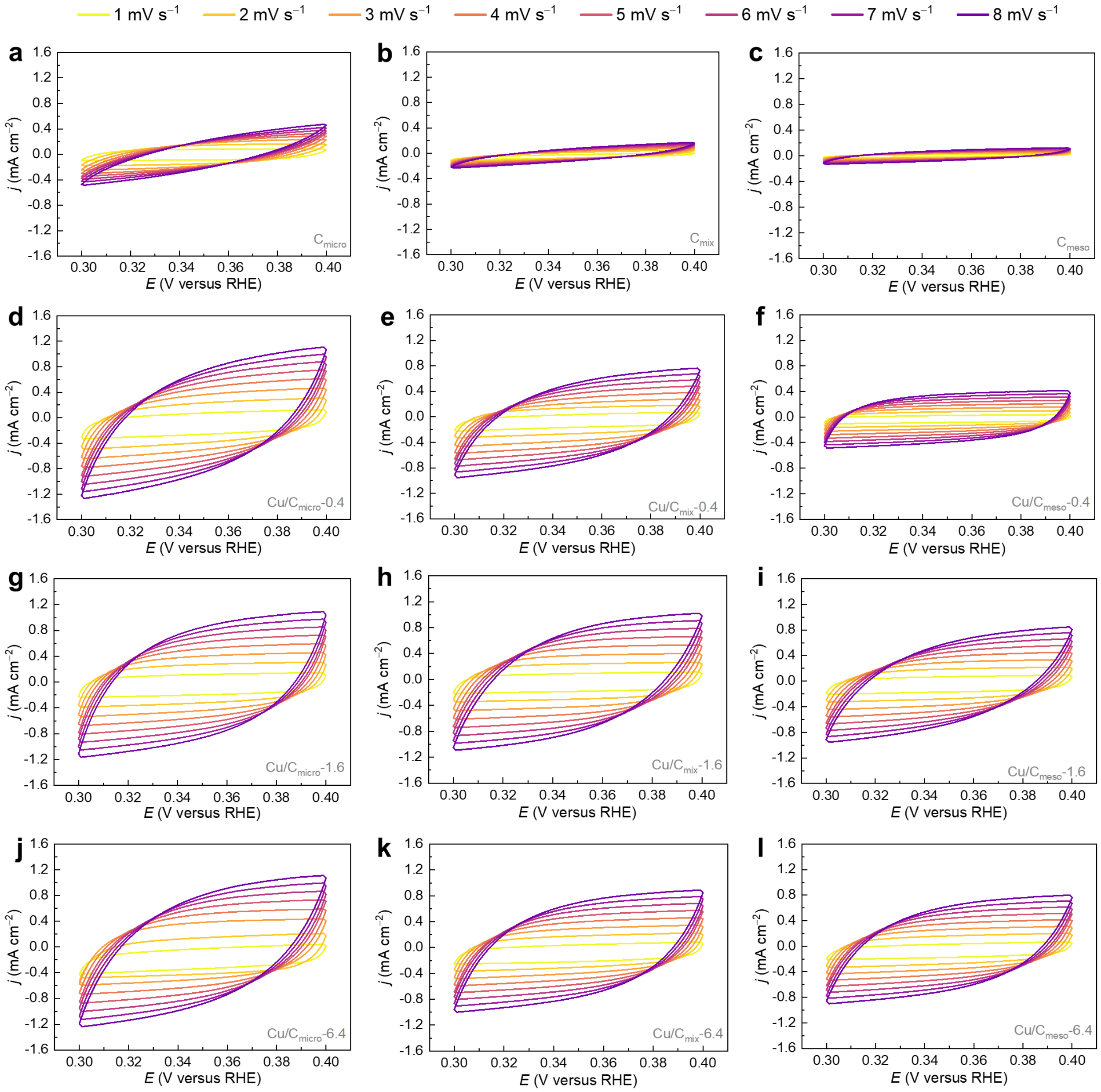

Supplementary Fig. 19 | Non-Faradaic region CV behavior at different scan rates (1 mV s^{-1} to 8 mV s^{-1}) **for varying Cu loadings on different carbon supports. a**. C$_{micro}$, **b.** C$_{mix}$, **c.** C$_{meso}$. **d.** Cu/ C$_{micro}$-0.4, **e.** Cu/ C$_{mix}$-0.4, **f.** Cu/ C$_{meso}$-0.4, **g.** Cu/ C$_{micro}$-1,6, **h.** Cu/ C$_{mix}$-1.6, **i.** Cu/ C$_{meso}$-1.6, **j.** Cu/ C$_{micro}$-6.4, **k.** Cu/ C$_{mix}$-6.4, **l.** Cu/ C$_{meso}$-6.4.

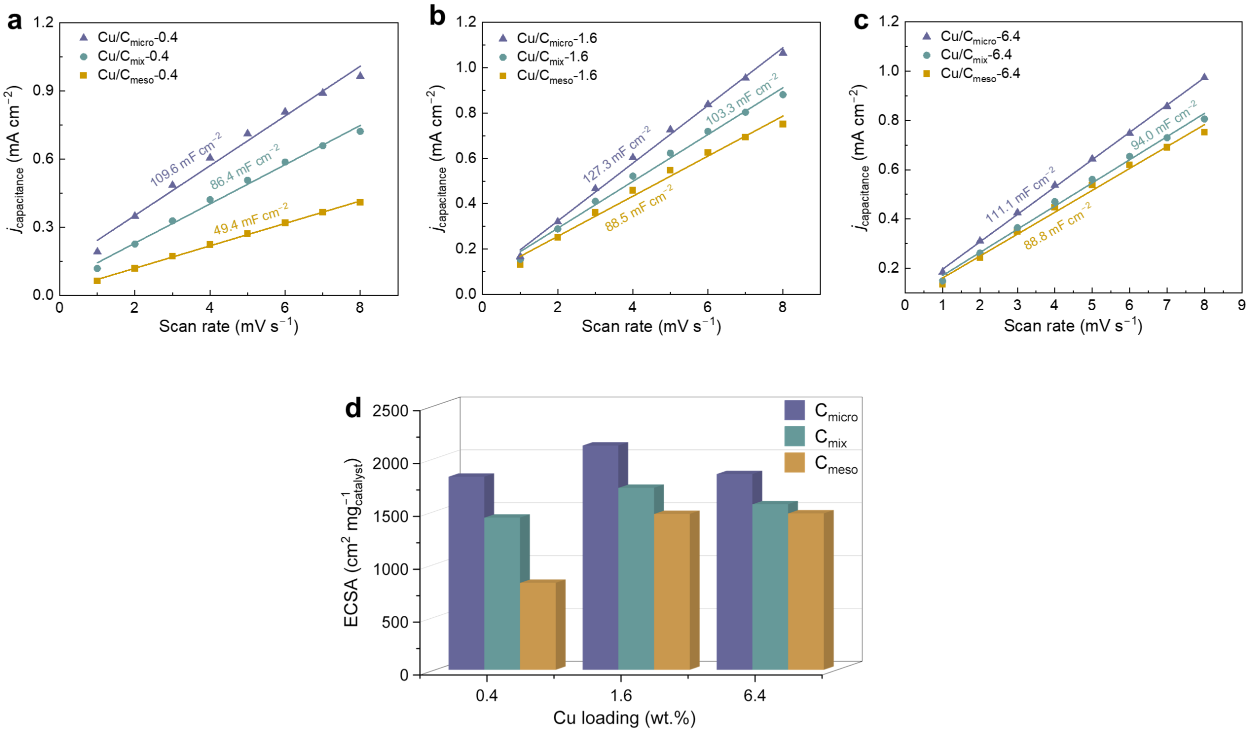

Supplementary Fig. 20 | Variations in electrochemical double-layer capacitance (EDLC) and electrochemical active surface area (ECSA) with varying Cu loading on different carbon supports. a-c. EDLC catalyzed by different Cu loadings on C$_{micro}$, C$_{mix}$, and C$_{meso}$, calculated based on **Supplementary Figure 19**. **d.** ECSAs of C$_{micro}$, C$_{mix}$, and C$_{meso}$ with different Cu loadings, calculated based on EDLC. Cu/C$_{micro}$ catalysts exhibit a highest ECSA due to higher surface area and microporosity at different loadings. However, the ECSA difference between three Cu/C catalysts becomes smaller while the Cu loading increases. This is because the larger Cu grains at higher loadings will partially cover the micropore entrances and level the ECSA of catalysts among different substates.

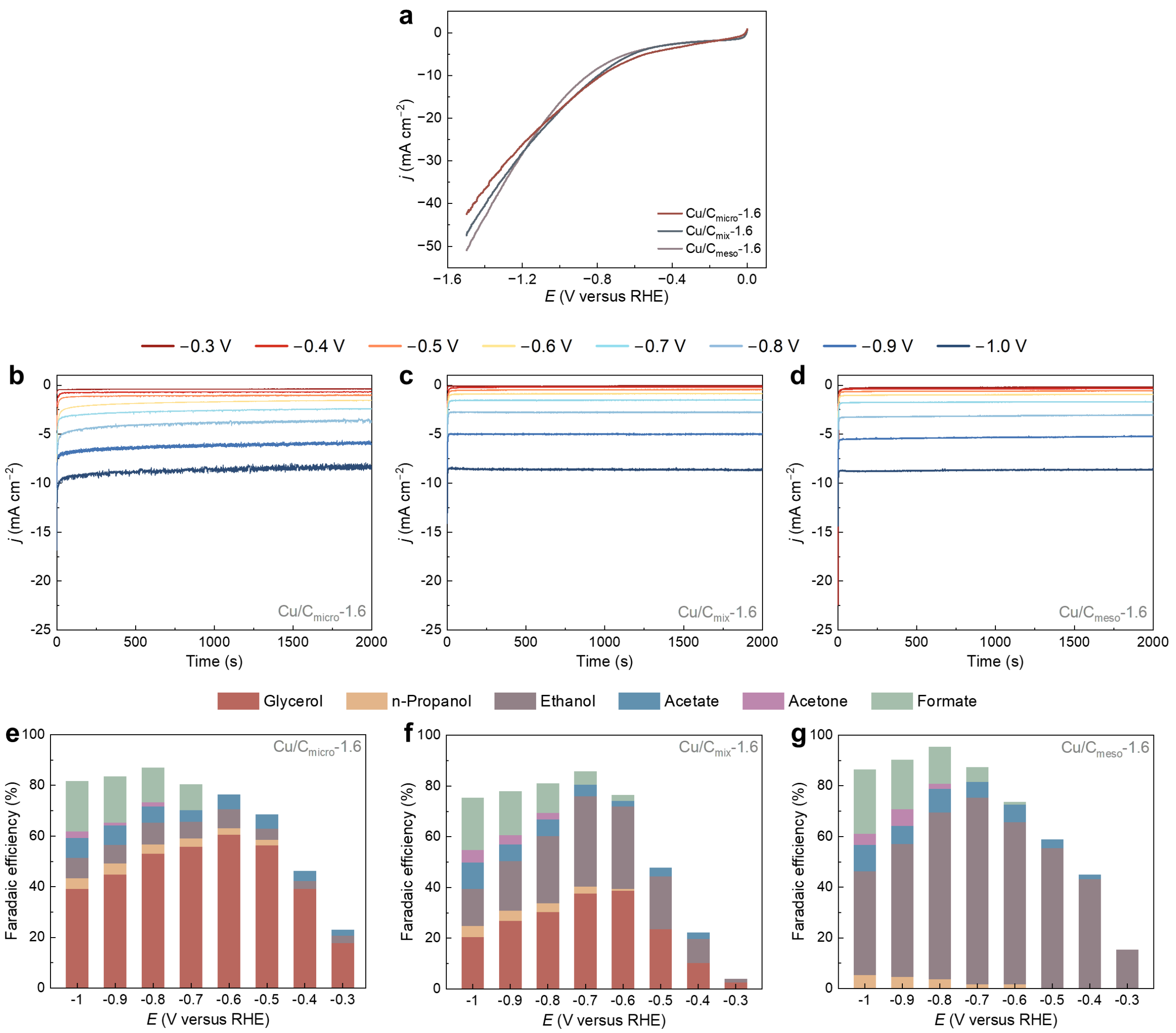

Supplementary Fig. 21 | eCO$_2$RR performance of Cu/C$_{micro}$-1.6, Cu/C$_{mix}$-1.6, and Cu/C$_{meso}$-1.6. LSVs of Cu/C$_{micro}$-1.6, Cu/C$_{mix}$-1.6, and Cu/C$_{meso}$-1.6 in **a.** CO$_2$-saturated 0.1 M KHCO$_3$ in a potential range of −0.3 to −1.0 V (Scan rate: 2 mV s^{-1}). **b-d.** The current density as the function of time for Cu/C$_{micro}$-1.6, Cu/C$_{mix}$-1.6, and Cu/C$_{meso}$-1.6 measured at different potentials during the chronoamperometry experiment. FEs and the product distribution of **e.** Cu/C$_{micro}$-1.6, **f.** Cu/C$_{mix}$-1.6 and **g.** Cu/C$_{meso}$-1.6 at disparate polarization potentials (*E*) versus RHE in CO$_2$-saturated 0.1 M KHCO$_3$.

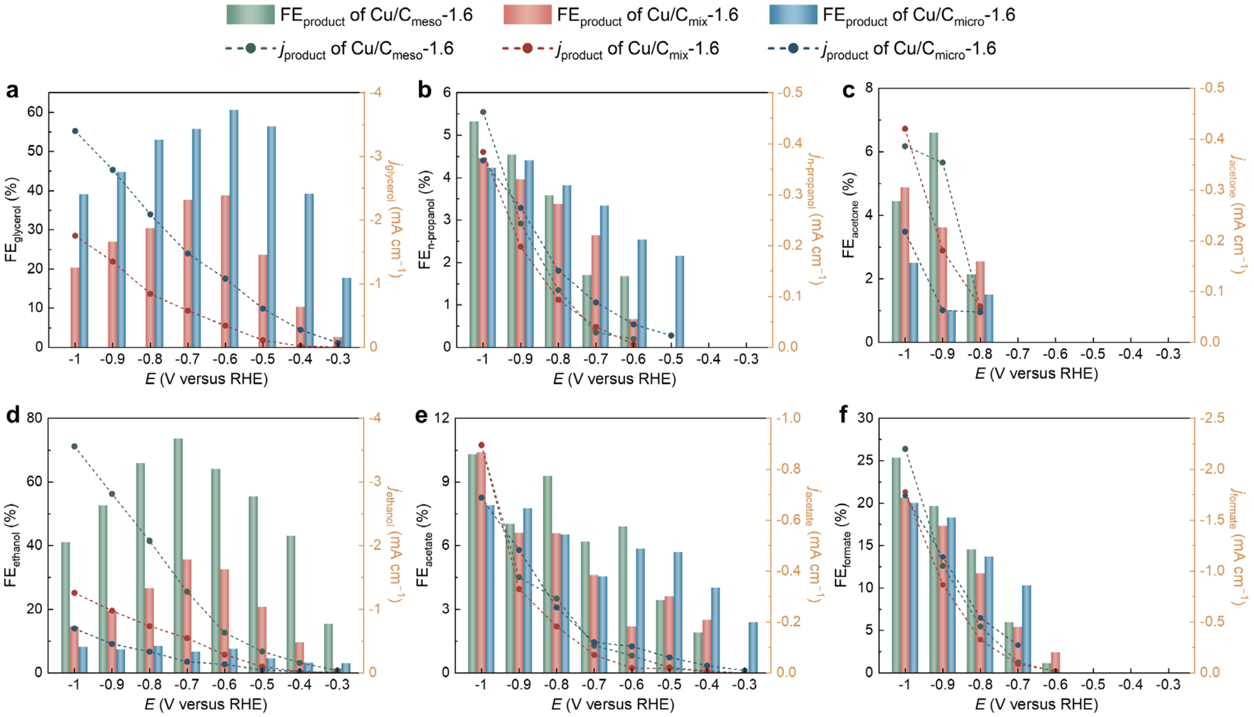

Supplementary Fig. 22 | Comparative analysis of partial FEs and partial j for specific products from Cu/C$_{micro}$-1.6, Cu/C$_{mix}$-1.6, and Cu/C$_{meso}$-1.6. a. glycerol. **b.** n-propanol. **c.** acetone. **d.** ethanol. **e.** ethylene. **f.** acetate. **g.** formate.

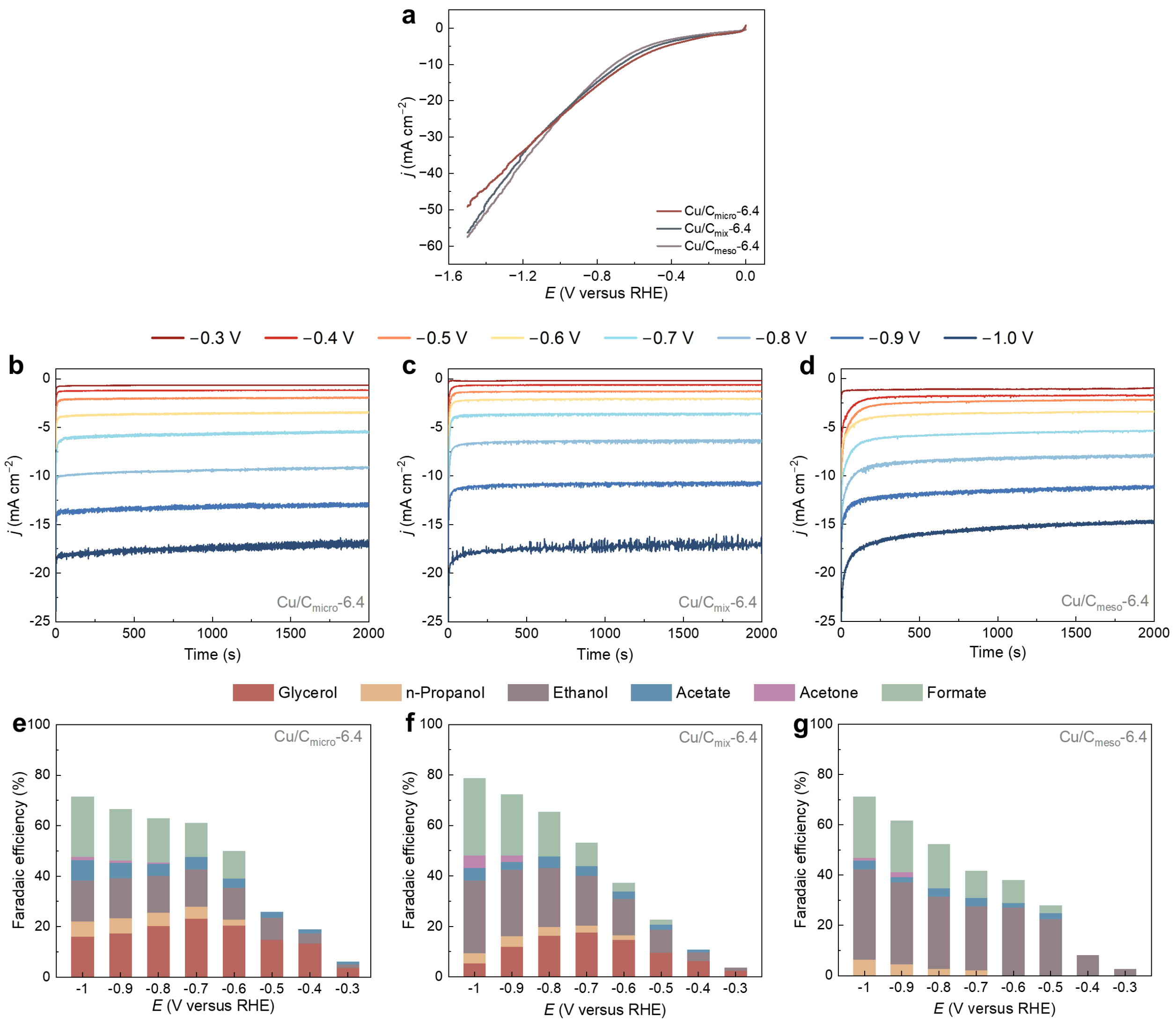

Supplementary Fig. 23 | CO_2RR performance of Cu/C$_{micro}$-6.4, Cu/C$_{mix}$-6.4, and Cu/C$_{meso}$-6.4. LSVs of Cu/C$_{micro}$-6.4, Cu/C$_{mix}$-6.4, and Cu/C$_{meso}$-6.4 in **a.** CO_2-saturated 0.1 M $KHCO_3$ in a potential range of −0.3 to −1.0 V (Scan rate: 2 mV s^{-1}). **b-d.** The current density as the function of time for Cu/C$_{micro}$-6.4, Cu/C$_{mix}$-6.4, and Cu/C$_{meso}$-6.4 measured at different potentials during the chronoamperometry experiment. FEs and the product distribution of **e.** Cu/C$_{micro}$-6.4, **f.** Cu/C$_{mix}$-6.4 and **g.** Cu/C$_{meso}$-6.4 at disparate polarization potentials (*E*) versus RHE in CO_2-saturated 0.1 M $KHCO_3$.

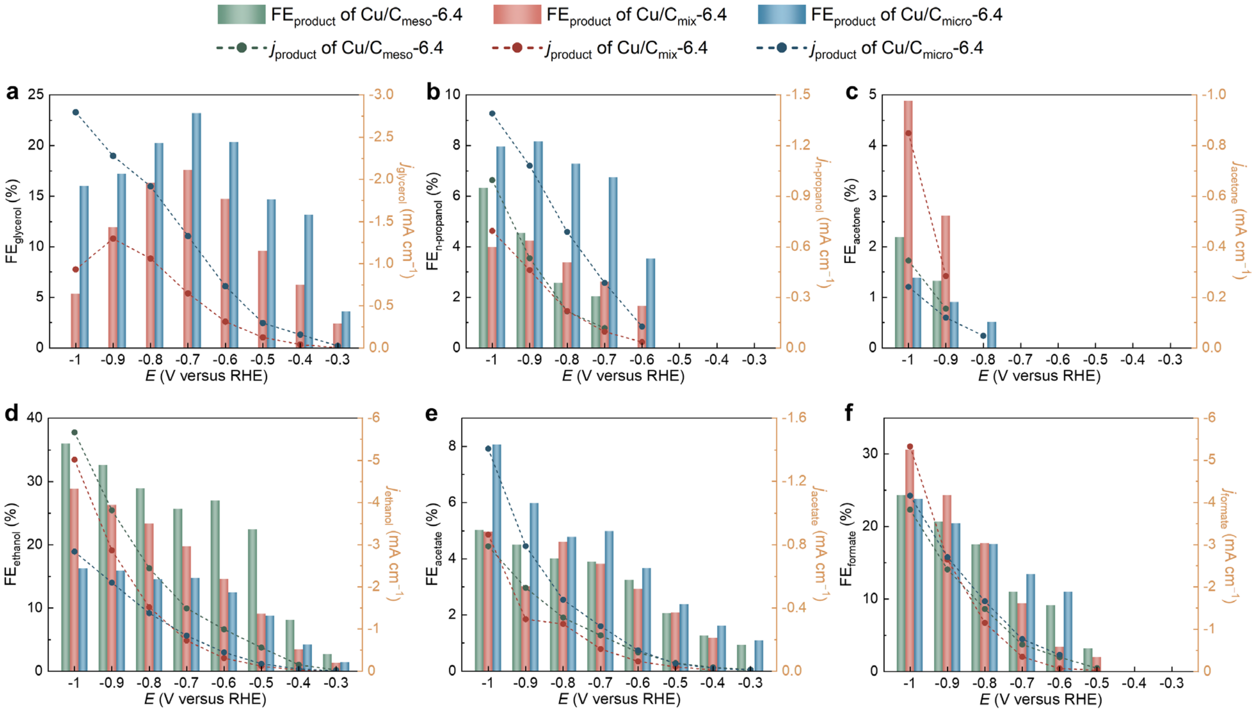

Supplementary Fig. 24 | Comparative analysis of partial FEs and partial *j* for specific products from Cu/C$_{micro}$-6.4, Cu/C$_{mix}$-6.4, and Cu/C$_{meso}$-6.4. a. glycerol. **b.** n-propanol. **c.** acetone. **d.** ethanol. **e.** ethylene. **f.** acetate. **g.** formate.

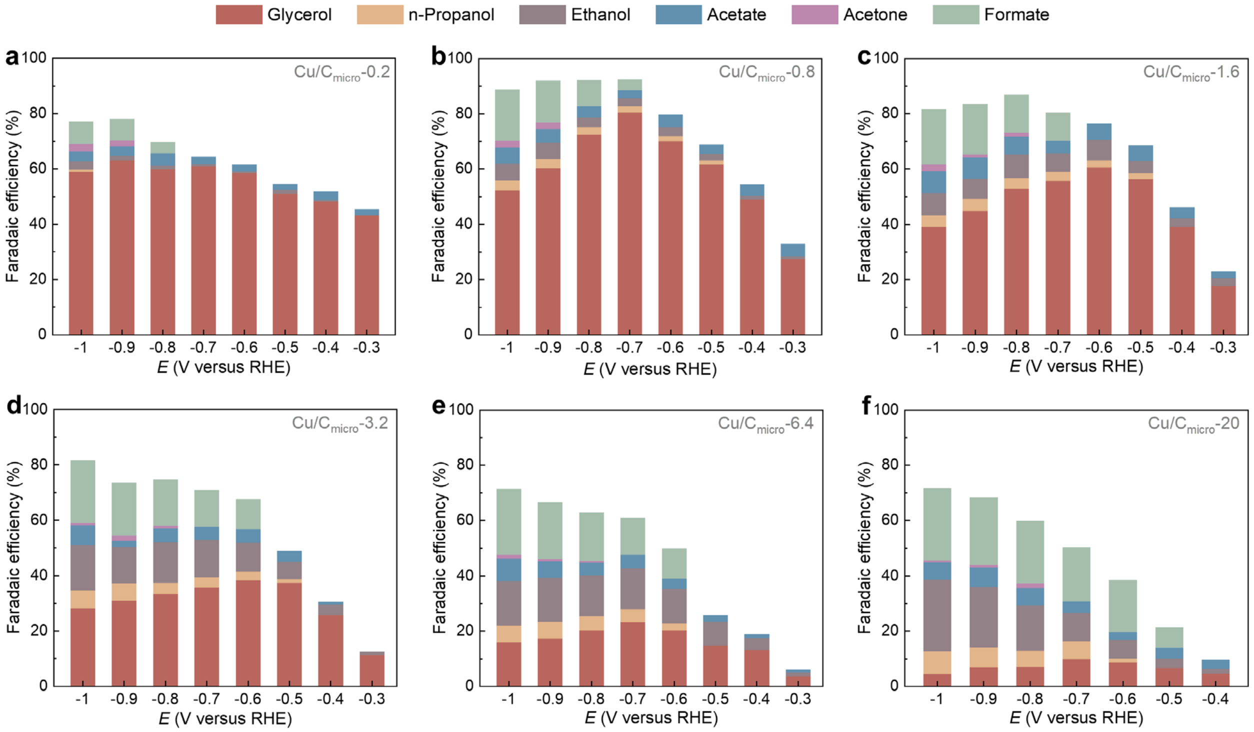

Supplementary Fig. 25 | Product distribution of CO_2RR from Cu/C$_{\text{micro}}$-*x* at different polarization potentials**. a.** Cu/C$_{\text{micro}}$-0.2, **b.** Cu/C$_{\text{micro}}$-0.8. **c.** Cu/C$_{\text{micro}}$-1.6. **d.** Cu/C$_{\text{micro}}$-3.2. **e.** Cu/C$_{\text{micro}}$-6.4. **f.** Cu/C$_{\text{micro}}$-20.

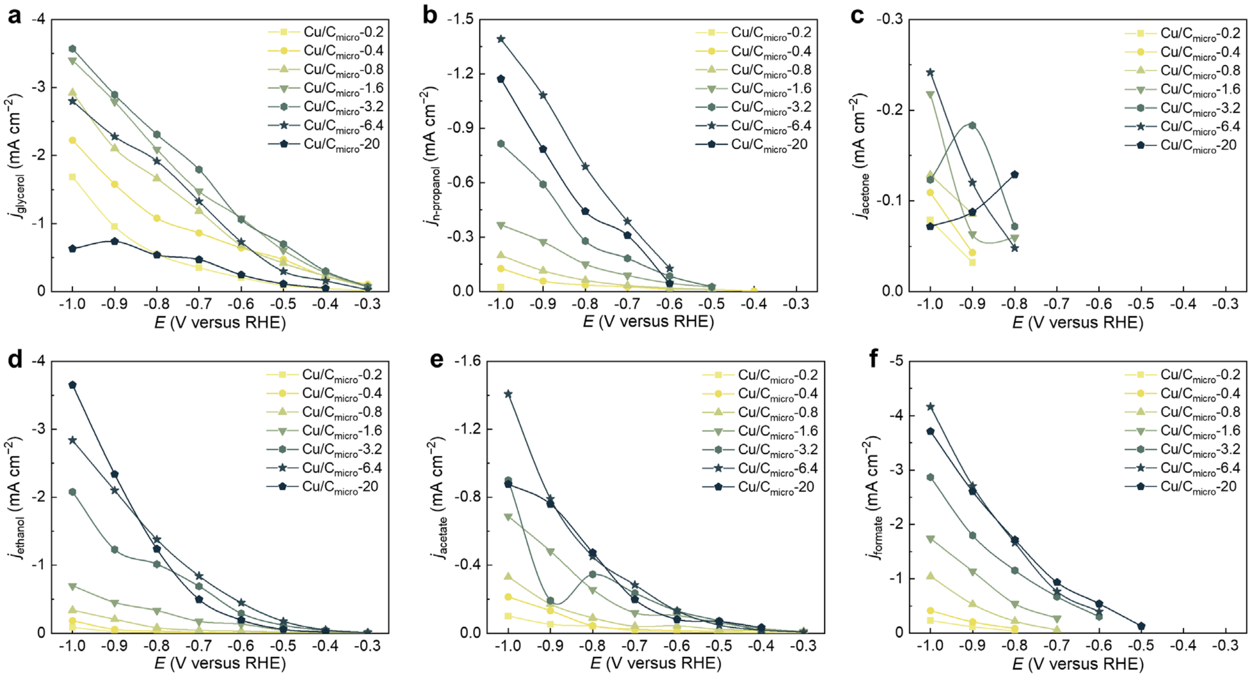

Supplementary Fig. 26 | Partial current densities of various products in CO_2RR catalyzed by Cu/C$_{micro}$-*x* at different polarization potentials. **a.** glycerol, **b.** n -propanol, **c.** acetone, **d.** ethanol, **e.** acetate, **f.** formate.

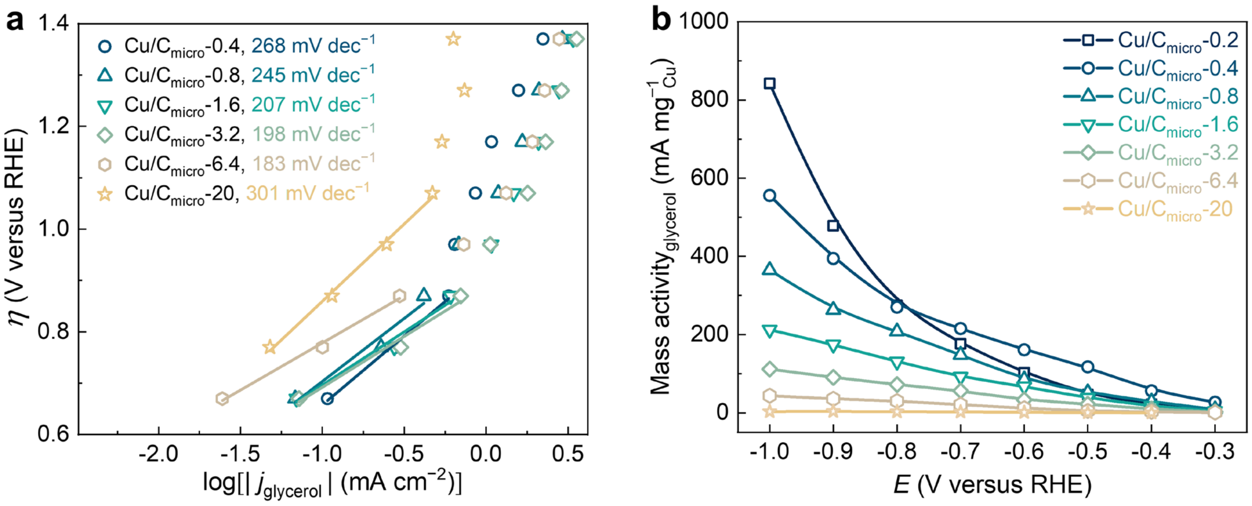

Supplementary Fig. 27 | Tafel plots and mass activities for the formation of glycerol which derived from the glycerol producing current density at different polarization overpotentials (η). **a.** Tafel plots of the formation of glycerol which derived from the glycerol producing current density at different polarization overpotentials (η). **b.** Mass activities analysis of glycerol in CO_2RR catalyzed by Cu/C$_{micro}$-*x* at different polarization potentials. Analysis of glycerol mass activity suggests that lower Cu loadings result in higher mass activities for glycerol production in CO_2RR, demonstrating an exceptionally high utilization efficiency of Cu to produce glycerol under lower Cu loading.

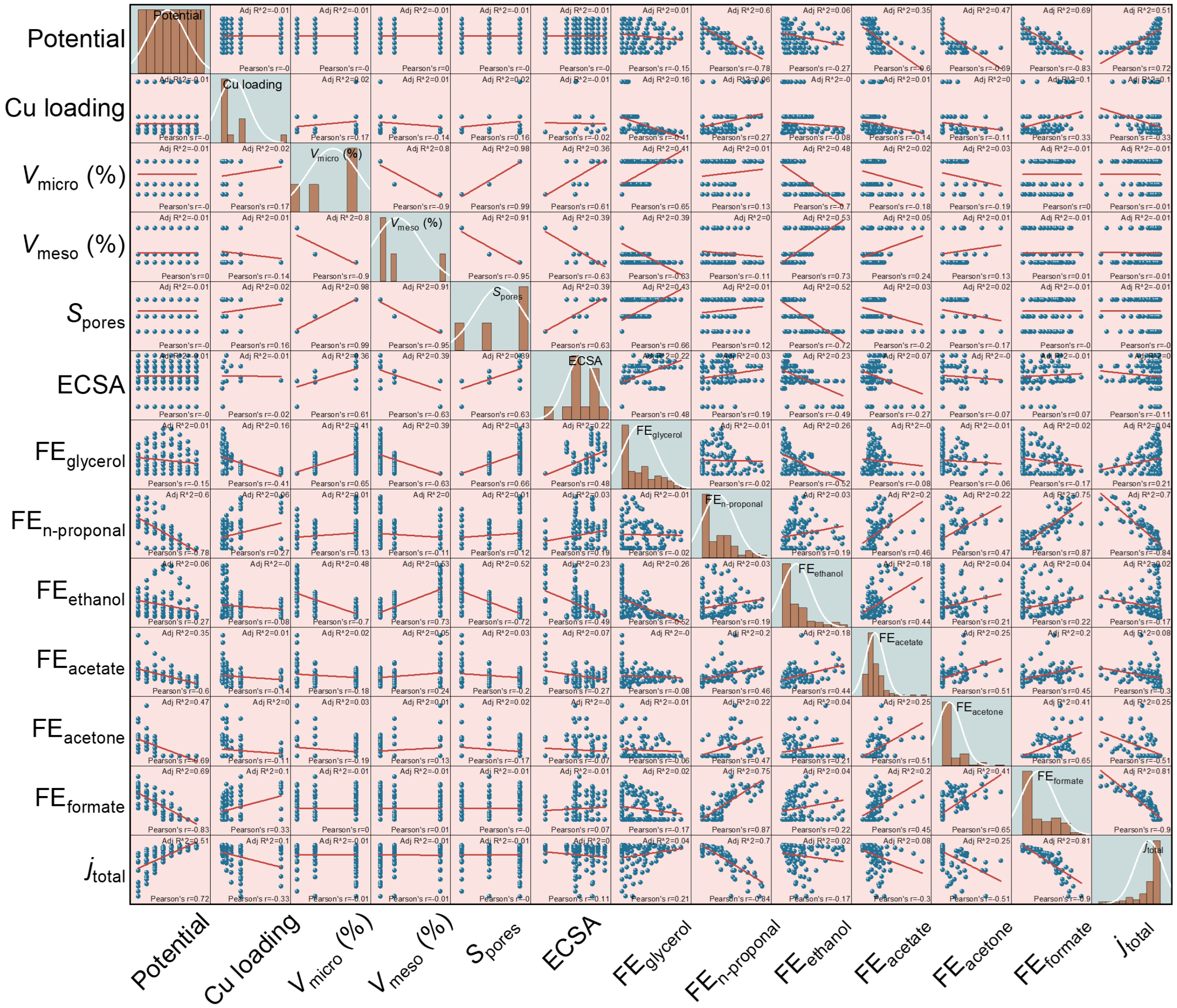

Supplementary Fig. 28 | Scatter matrix of electrocatalytic properties for Cu/C-*x*. The scatter matrix is constructed based on the correlation matrix and provides a graphical representation of these pairwise relationships through scatter plots. The diagonal sections (cyan background) of the scatter matrix typically exhibit the distribution of each variable either through histograms (earthy yellow bar) and kernel density estimation (white line), facilitating observations of variable distributions. Histograms can reveal the skewness, kurtosis, and conformity to normal distribution of a variable; kernel density estimation curves provide a smooth visualization of the data density distribution. The graphical representations on the diagonal can assist in evaluating the normality of the data and the presence of outliers. The cells off the diagonal in the scatter matrix are scatter plots of each pair of variables (blue dot), used to observe patterns in their relationships: If the data points are aligned in a straight line, this indicates a high linear correlation between the variables. If the data points form a curved pattern, this suggests a potential nonlinear relationship between the variables. If there are data points that significantly deviate from the main cluster, these may represent outliers. The red lines overlaying each scatter plot are fitted trend lines, specifically the result of a linear regression fit for the two variables in that cell. In practice, this red line is essentially a linear regression line that summarizes the relationship between the x and y axes in that cell. Each red line by fitting a straight-line model $y = a + bx$ to the data in that scatter plot cell, where a is the intercept and b is the slope. The direction of correlation is evident from the sign of r and the slope of the line ($+$ or $-$), while the strength is indicated by the magnitude of r or R^2 and how scattered the points are around the red line.

This Pearson correlations encompasses data from 104 independent experiments conducted in this study. Pearson's correlation coefficient measures only pairwise associations between two variables and cannot capture interactions between multiple features. If CO_2RR performance depends on a combination of support properties (such as an optimal balance of micropore and mesopore content), simple correlations of each property with performance will not reflect this joint effect.

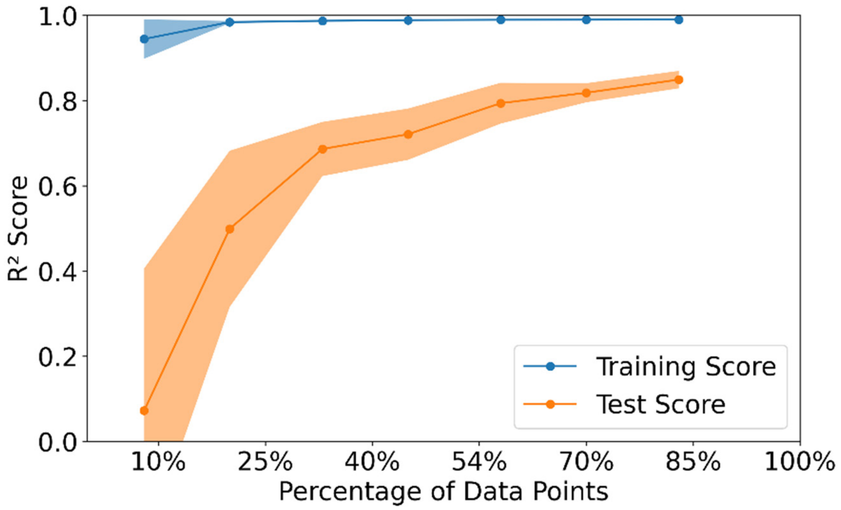

Supplementary Fig. 29 | Learning curve of predictive models. The test dataset contained 20% of the selected dataset for each training case. The shaded region represents one standard deviation which was calculated from K-fold cross-validation of 5-folds. The complete dataset contains 104 total number of datapoints. The figure shows the learning curve of the predictive models where models were trained with increasing amount of data. For small amount of data (< 25%), the training score is significantly higher than the test score. Adding more data improved the test score and the models quickly reached close to their optimum performance when trained with 80% of the complete dataset. Note, the number of datapoints available in the complete dataset is only 104 datapoints which is considered to be a very small dataset for machine learning purposes. Despite the small size of the dataset, achieving an R^2 score higher than 0.8 demonstrates the predictive capability of the XGB regressor model and highlights the high correlation among the features and the target faradaic efficiencies.

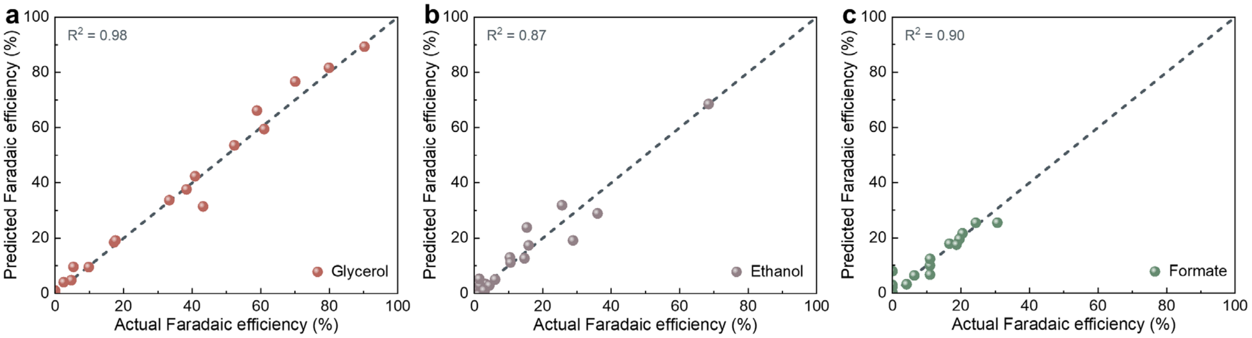

Supplementary Fig. 30 | Model predicted *vs.* actual FEs for **a.** glycerol, **b.** ethanol, **c.** formate in the test dataset. The black dotted line shows the ideal case of perfect predictions.

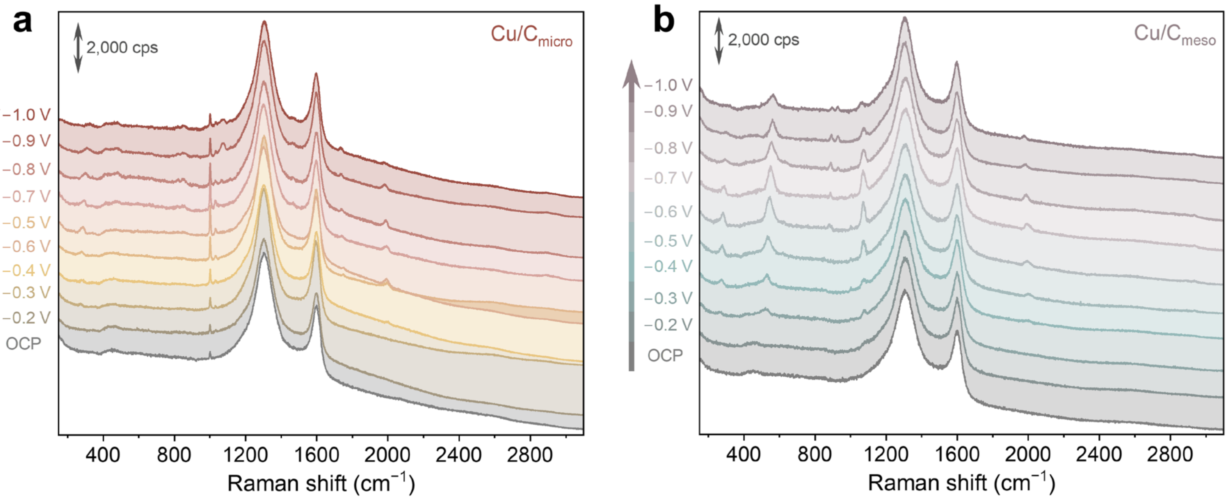

Supplementary Fig. 31 | Full *in situ* EC-SHINERS measurement in CO_2 saturated 0.1 M $KHCO_3$. **a.** Cu/C$_{micro}$ and **b.** Cu/C$_{meso}$ during stepwise decrease of the potential from OCP to −1.0 V**.**

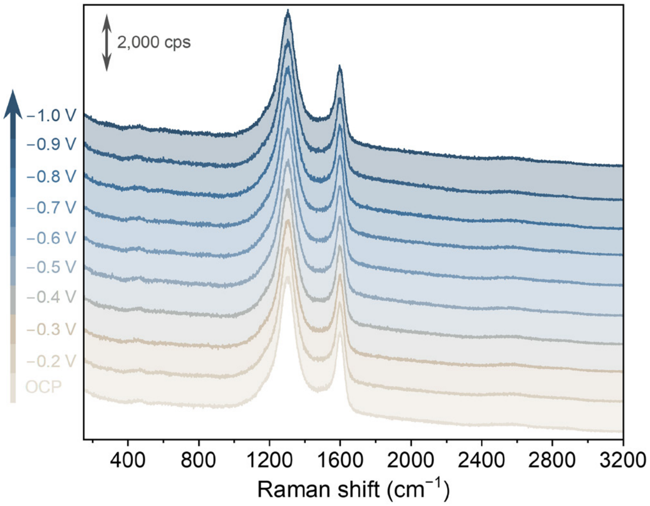

Supplementary Fig. 32 | Full *in situ* EC-SHINERS measurement for blank C$_{micro}$ in CO_2 saturated 0.1 M $KHCO_3$.

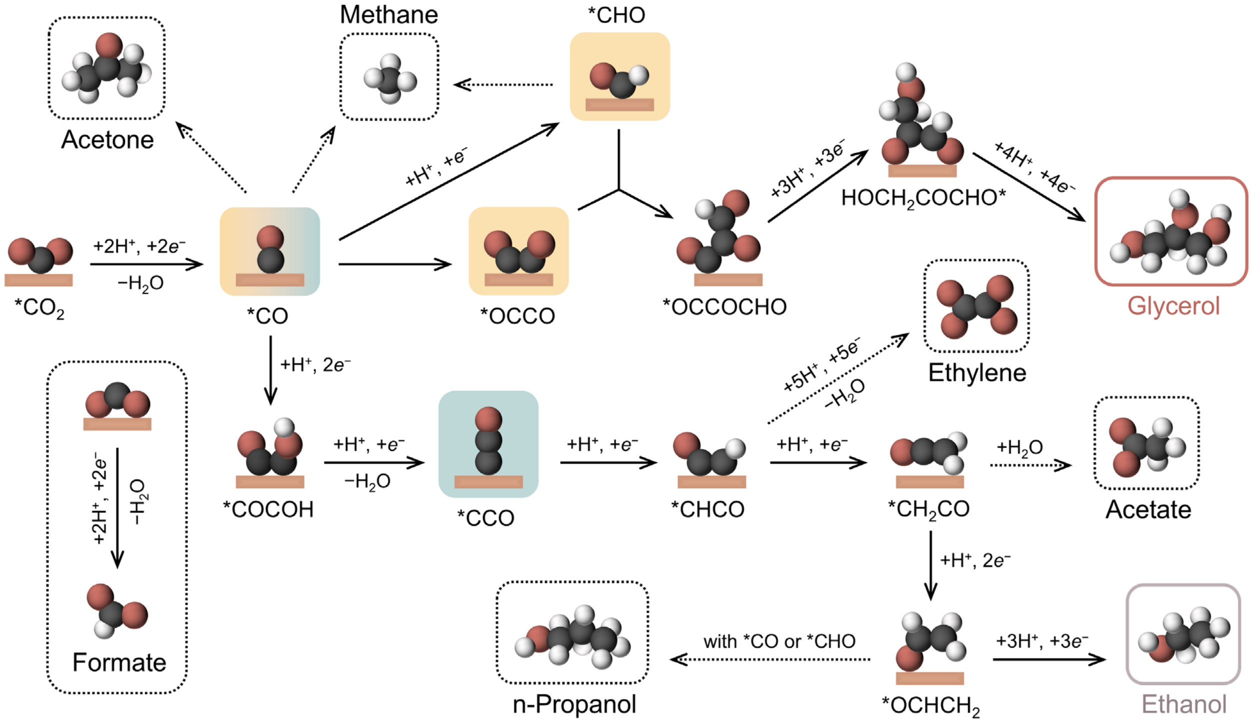

Supplementary Fig. 33 | Proposed full mechanism for the electroreduction of CO_2 to glycerol and ethanol and other by-products over Cu/C_{micro} and Cu/C_{meso} catalyst systems. The key byproducts in the ethanol pathway, such as ethylene and acetate are all detected in the electrochemical tests and are present at much higher concentrations in Cu/C_{meso} than in Cu/C_{micro}. This supports the notion that these byproducts and ethanol share a common *C=C=O pathway, which is distinct from that of glycerol. Additionally, these products show a clear competitive relationship with ethanol across different potentials, consistent with our proposed reaction mechanism. Minor byproducts such as methane and acetone, likely derived from *CO or *CO trimerization, are detected in both systems and are less influenced by nanoconfinement. At sufficiently negative potentials, the CO_2 adsorption mode changes due to kinetic control, leading to increased formate formation, a trend common to both systems. In summary, the high glycerol selectivity observed in Cu/C_{micro} is attributed to the coupling of *OCCO and *CHO intermediates enabled by nanoconfinement, while the Cu/C_{meso} catalyst, which lacks such confinement, exhibits catalytic behavior similar to that previously reported Cu-based systems.

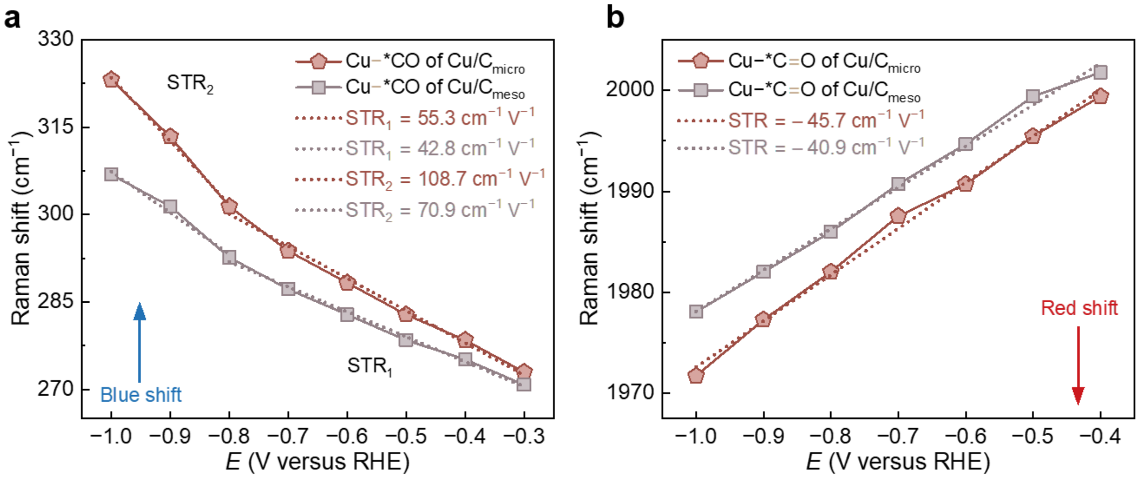

Supplementary Fig. 34 | Stark effect and stark tunning rate. Relationship comparison between Raman shifts of **a.** Cu−C vibration of Cu−*CO and reduction potential, and **b.** C=O vibration in Cu−*CO and reduction potential in eCO$_2$RR over Cu/C$_{micro}$ and Cu/C$_{meso}$, respectively. STR$_1$ and STR$_2$ mean the stark tunning rate calculated from −0.3 V to −0.8 V and −0.8 V to −1.0 V, respectively. STR$_2$ reflect the condition which a second order polarizability Δα took into effect.

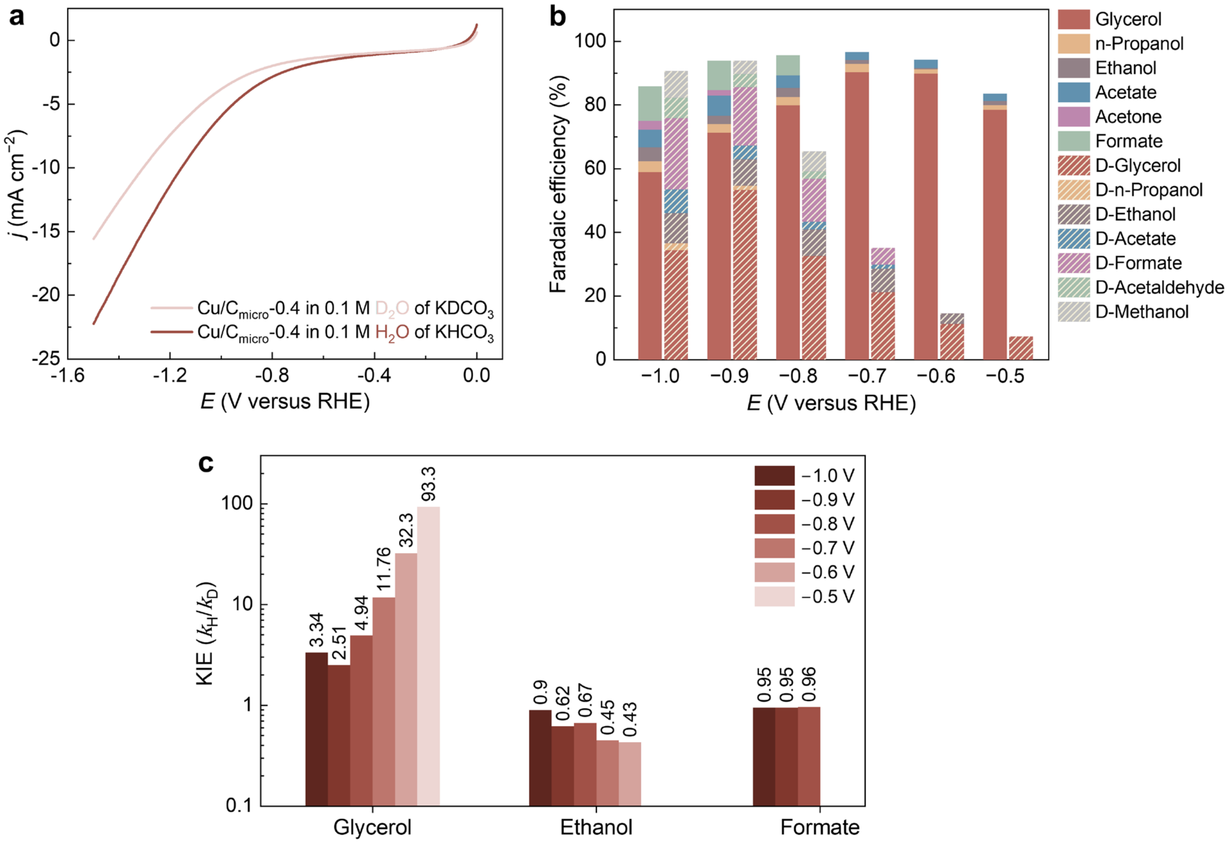

Supplementary Fig. 35 | KIE electrochemical test results of Cu/C$_{micro}$-0.4 in 0.1 M D_2O of $KDCO_3$. **a.** LSV curves (scan rate 10 mV s^{-1}) in 0.1M $KHCO_3/H_2O$ and 0.1 M $KDCO_3/D_2O$ electrolyte with CO_2 purge. Due to the slower kinetics of D compared to H, we observed in LSV that the current density of Cu/C$_{micro}$-0.4 in 0.1 M $KDCO_3/D_2O$ increased more slowly as the potential decreased, compared to its behavior in 0.1 M $KHCO_3/H_2O$. **b.** Comparison of FEs and product distributions at different electrochemical potentials between CO_2RR over 0.1 M $KHCO_3/H_2O$ based electrolyte (clear bar) and 0.1 M $KDCO_3/D_2O$ based electrolyte (shaded bar) over Cu/C$_{micro}$-0.4 electrocatalyst. FEs product distribution is completely changed, and the onset potential for the CO_2RR on Cu/C$_{micro}$-0.4 in 0.1 M $KDCO_3/D_2O$ is shifted to −0.5 V, with no CO_2RR-related products detected at −0.4 V. **e.** KIE of CO_2RR to glycerol, n-propanol, ethanol, acetate and formate over Cu/C$_{micro}$-0.4. In KIE experiments employing deuterated electrolytes, all potentials are referenced to the RHE scale to facilitate comparison of KIEs. Consequently, an additional correction of 44 mV is applied in the potential conversion calculations for the $KDCO_3/D_2O$ electrolyte, reflecting the difference between $pK_w^H = 14$ and $pK_w^D = 14.95$. Thus, the $pD = pH \times 1.068$ and included in the potential measurements[24].

Supplementary Tables

Supplementary Table 1 | Comparative analysis of pore characteristics in C_{micro}, C_{mix}, and C_{meso}.

	$\mathbf{C_{micro}}$	$\mathbf{C_{mix}}$	$\mathbf{C_{meso}}$
BET specific surface area (m^2 g^{-1})	2015	1540	1392
Total area in pores (m^2 g^{-1})	1511	1175	875
S_{micro} (m^2 g^{-1})	1297	649	137
$S_{porous < 3\ nm}$ (m^2 g^{-1})	1483	709	250
S_{meso} (m^2 g^{-1})	214	105	402
Ratio of S_{micro} : S_{total} in pores (%)	85.8	55.2	15.7
Ratio of $S_{porous < 3\ nm}$: S_{total} in pores (%)	98.1	67.7	28.6
Ratio of S_{meso} : S_{total} in pores (%)	14.2	9	45.9
Total volume in pores (cm^3 g^{-1})	0.85	1.3	1.2
V_{micro} (cm^3 g^{-1})	0.59	0.34	0.08
$V_{porous < 3\ nm}$ (cm^3 g^{-1})	0.8	0.42	0.23
V_{meso} (cm^3 g^{-1})	0.26	0.56	1.02
Ratio of V_{micro} : V_{total} in pores (%)	69	26	7
Ratio of $V_{porous < 3\ nm}$: V_{total} in pores (%)	94	32	19
Ratio of V_{meso} : V_{total} in pores (%)	30	43	85

From the N_2 adsorption isotherm obtained at 77 K, information related to the pore size distribution of the sample was extracted using the 2D-NLDFT method. Definitions for the pores: micropores have a diameter less than 2 nm, mesopores range from 2 nm to 50 nm, and macropores are those greater than 50 nm.

Supplementary Table 2 | Thermodynamic parameters of CO_2 adsorption.

	C_{micro}	**C_{mix}**	**C_{meso}**
CO_2 adsorption capacity @ one bar and 273 K (q_{273}) (mmol g^{-1})	5.08	3.63	2.10
CO_2 adsorption capacity @ one bar and 297 K (q_{297}) (mmol g^{-1})	2.48	1.91	1.31
$-\Delta H^{a}_{\text{ads}}$ (kJ mol^{-1}) @ CO_2 uptake onset	34.3	30.1	26.9
$-\Delta H^{b}_{\text{ads}}$ (kJ mol^{-1}) @ CO_2 uptake = 1 mmol g^{-1}	24.7	21.1	19.7
$-\Delta S^{a}_{\text{ads}}$ (J mol^{-1} K^{-1}) @ CO_2 uptake onset	97.3	86.0	83.0
$-\Delta S^{b}_{\text{ads}}$ (J mol^{-1} K^{-1}) @ CO_2 uptake = 1 mmol g^{-1}	82.8	75.7	74.9

Supplementary Table 3 | Raman shift of CO_2 in three carbons.

	Gaseous CO_2	**CO_2@C_{meso}**	**CO_2@C_{mix}**	**CO_2@C_{micro}**
$F_{\nu-}$ (cm^{-1})	1285.93	1284.27	1283.83	1282.94
$F_{\nu+}$ (cm^{-1})	1388.34	1386.78	1386.34	1385.47
$\Delta F_{\nu-}$ (cm^{-1})	0	1.66	2.1	2.99
$\Delta F_{\nu+}$ (cm^{-1})	0	1.56	2	2.87

Supplementary Table 4 | XRF and EDX quantitative analysis. The actual Cu loadings of the catalyst were determined through rigorous analysis using XRF and EDX measurements.

Catalysts	Nominal loading (wt.%)	XRF analysis (wt.%)		EDX analysis (wt.%)		
	Cu	Cu	O	Cu	O	C
Cu/C_{micro}-0.2	0.2	0.21	99.79	0.22	4.83	94.95
Cu/C_{micro}-0.4	0.4	0.39	99.61	0.39	4.91	94.7
Cu/C_{micro}-0.8	0.8	0.74	99.26	0.76	5.02	94.22
Cu/C_{micro}-1.6	1.6	1.41	98.59	1.5	5.33	93.17
Cu/C_{micro}-3.2	3.2	3.01	96.99	2.91	7.64	89.45
Cu/C_{micro}-6.4	6.4	5.24	94.76	5.53	10.11	84.36
Cu/C_{micro}-20	20	15.11	84.89	15.66	16.07	68.27
Cu/C_{mix}-0.4	0.4	0.42	99.58	0.42	3.45	96.13
Cu/C_{mix}-1.6	1.6	1.32	98.68	1.45	4.46	94.09
Cu/C_{mix}-6.4	6.4	5.94	94.06	5.28	7.72	87
Cu/C_{meso}-0.4	0.4	0.35	99.65	0.36	3.49	96.15
Cu/C_{meso}-1.6	1.6	1.37	98.63	1.42	4.49	94.09
Cu/C_{meso}-6.4	6.4	6.15	93.85	5.65	8.21	86.14

The actual Cu loading employed for data analysis is examined. It is expected that the loading is lower than the nominal value, which can be attributed to two factors. Firstly, the weight of the carbon support increases due to the addition of O-containing functional groups through LiOH water washing. Secondly, during the synthesis process, the conversion of Cu to CuO compounds takes place, resulting in a reduction in the weight percentage of Cu. This tendency becomes more pronounced as the copper loading is increased. The elements that are lighter on the periodic table, such as C and O, emit X-rays that are too weak to travel back to the detector and be counted. Therefore, the weight percentages of light elements other than copper are all considered as contributions from carbon weight.

Supplementary Table 5 | Fitting parameters of Cu K-edge EXAFS spectra.

Sample	**Path**	**R (Å)**	**CN**	**$\sigma^2\times10^{-3}$(Å^2)**	**R factor**
Cu/C$_{micro}$-0.4	Cu-O	1.922 ± 0.003	3.16 ± 0.10	1.87	0.006
Cu/C$_{mix}$-0.4	Cu-O	1.941 ± 0.002	3.02 ± 0.13	2.93	0.004
Cu/C$_{meso}$-0.4	Cu-O	1.949 ± 0.008	2.86 ± 0.13	2.38	0.003

The processing and analysis of X-ray Absorption Spectroscopy (XAS) data were performed using the ATHENA and ARTEMIS software packages. All spectra were calibrated, background-subtracted, and normalized in accordance with the protocols detailed in the ATHENA documentation. Based on the well-established local structures of Cu(AcAc)$_2$, the Extended X-ray Absorption Fine Structure (EXAFS) spectra were fitted under the assumption of first-shell coordination numbers (CN). The Debye-Waller factor (σ^2) was included to represent disorder in bond distances. All fittings were conducted in R-space with a k-weight of 3. The fitting ranges for Cu were defined as $3 \leq k(\text{Å}^{-1}) \leq 12$, and $1.0 \leq \text{R(Å)} \leq 2.0$.

Supplementary Table 6 | Optimized hyperparameters and the explored parameter space for the final regressor models.

Parameter	Optimized value	Range tested (interval)
Number of trees	250	100 – 1100 (200)
Maximum tree depth	5	3 – 11 (2)
Learning rate	0.2	0.01, 0.125, 0.2
Subsample ratio of the training instance	0.5	0.5 – 1 (0.1)
Subsample ratio of columns when constructing each tree	0.8	0.5 – 1 (0.1)
Gamma	0	0 – 2 (0.5)

The optimized model hyperparameters found through the random search cross-validation algorithm in Scikit-learn are reported in Table. After identifying the optimal hyperparameters, the dataset was shuffled and the final models were trained on 80% of the dataset, leaving 20% of the data for testing the predictive performance of the models. The Evaluation metrics of choice to quantify model performance in this work was the coefficient of determination or, R^2 Score. The dataset along with all code used to analyze the data and train the models will be made available on Github[25].

Supplementary Table 7 | Raman band observed by *in situ* electrochemical SHINERS.

Frequency (cm^{-1})	**Assignment**	**Cu/C$_{\text{micro}}$**	**Cu/C$_{\text{meso}}$**	**Stark effect**	**$\Delta\mu$ (cm^{-1}/V)**	**Reference**
273.0 – 323.14	Cu–*CO	✓		✓$_{+}$	55.3 (STR$_1$) 108.7 (STR$_2$)	26
270.81 – 306.85	Cu–*CO		✓	✓$_{+}$	42.8 (STR$_1$) 70.9 (STR$_2$)	26
520.55 – 563.37	Cu–*(OH)C=CHO or Cu–*C=C=O		✓	✓$_{+}$	63.4	27,28
813.64 – 823.57	unassigned	✓		✓$_{+}$	25.8	
844.38 – 857.22	unassigned	✓		✓$_{+}$	31.6	
877.9 – 897.52	unassigned		✓	✓$_{+}$	48.1	
925.85 – 931.69	unassigned		✓	✓$_{+}$	29.2	
1002.26	HCO_3^-	✓	✓			
1021.43–1034.81	Cu–*CHO	✓		✓$_{+}$	15.7	28
1070.96	CO_3^{2-}	✓	✓			
1456.46 – 1467.88	Cu*OC−CO	✓		✓$_{-}$	37.8	26
1732.95 –1750.4	Cu–CHO–Cu	✓		✓$_{-}$	31.5	29
1971.74 – 1999.4	Cu*C=O	✓		✓$_{-}$	45.7	26
1978.08 – 2001.76	Cu*C=O		✓	✓$_{-}$	40.9	26
2820 – 3010	–C–H$_x$	✓	✓			

Supplementary References

1 Brunauer, S. et al. Adsorption of Gases in Multimolecular Layers. *J. Am. Chem. Soc.* **60**, 309-319 (1938).

2 Neimark, A. V. et al. Bridging scales from molecular simulations to classical thermodynamics: densityfunctional theory of capillary condensation in nanopores. *J. Phys.: Condens. Matter* **15**, 347 (2003).

3 Mason, J. A. et al. Evaluating metal–organic frameworks for post-combustion carbon dioxide capture via temperature swing adsorption. *Energy Environ. Sci.* **4**, 3030-3040 (2011).

4 van't Hoff, M. J. H. Etudes de dynamique chimique. *Recl. Trav. Chim. Pays-Bas* **3**, 333-336 (1884).

5 Clausius, R. Ueber die bewegende Kraft der Wärme und die Gesetze, welche sich daraus für die Wärmelehre selbst ableiten lassen. *Ann. Phys.* **155**, 368-397 (1850).

6 Ravel, B. et al. ATHENA, ARTEMIS, HEPHAESTUS: data analysis for X-ray absorption spectroscopy using IFEFFIT. *J. Synchrotron Radiat.* **12**, 537-541 (2005).

7 Xu, H. et al. Highly selective electrocatalytic CO_2 reduction to ethanol by metallic clusters dynamically formed from atomically dispersed copper. *Nat. Energy* **5**, 623-632 (2020).

8 Xu, H. et al. Modulating CO_2 Electrocatalytic Conversion to the Organics Pathway by the Catalytic Site Dimension. *J. Am. Chem. Soc.* **146**, 10357-10366 (2024).

9 Westheimer, F. The magnitude of the primary kinetic isotope effect for compounds of hydrogen and deuterium. *Chem. Rev.* **61**, 265-273 (1961).

10 Trasatti, S. et al. Real surface area measurements in electrochemistry. *Pure Appl. Chem.* **63**, 711-734 (1991).

11 McCrory, C. C. et al. Benchmarking heterogeneous electrocatalysts for the oxygen evolution reaction. *J. Am. Chem. Soc.* **135**, 16977-16987 (2013).

12 van der Heijden, O. et al. Tafel slope plot as a tool to analyze electrocatalytic reactions. *ACS Energy Lett.* **9**, 1871-1879 (2024).

13 Zhu, W. et al. Monodisperse Au nanoparticles for selective electrocatalytic reduction of CO_2 to CO. *J. Am. Chem. Soc.* **135**, 16833-16836 (2013).

14 Kuhl, K. P. et al. New insights into the electrochemical reduction of carbon dioxide on metallic copper surfaces. *Energy Environ. Sci.* **5**, 7050-7059 (2012).

15 Pearson, K. VII. Note on regression and inheritance in the case of two parents. *Proc. R. Soc. Lond. A* **58**, 240-242 (1895).

16 Blyth, S. Karl Pearson and the correlation curve. *Int. Stat. Rev.* 393-403 (1994).

17 Chen, T. et al. in *Proceedings of the 22nd ACM SIGKDD International Conference on Knowledge Discovery and Data Mining* 785–794 (Association for Computing Machinery, San Francisco, California, USA, 2016).

18 Chen, T. & Guestrin, C. *XGBoost: Machine Learning Challenge Winning Solutions.* GitHub. Available at: https://github.com/dmlc/xgboost/tree/master/demo#machine-learning-challenge-winning-solutions (accessed 12 Aug 2025).

19 Fabian, P. Scikit-learn: Machine learning in Python. *J. Mach. Learn. Res. 12*, 2825 (2011).

20 Fermi, E. Über den ramaneffekt des kohlendioxyds. *Z. Phys.* **71**, 250-259 (1931).

21 Bermúdez-Montaña, M. et al. An algebraic alternative for the accurate simulation of CO_2 Raman spectra. *J. Raman Spectrosc.* **51**, 569-583 (2020).

22 Scherrer, P. Nachr Ges wiss goettingen. *Math. Phys.* **2**, 98-100 (1918).

23 Cullity, B. D. et al. Elements of X-ray Diffraction. *Phys. Today* **10**, 50-50 (1957).

24 Krężel, A. et al. A formula for correlating pKa values determined in D_2O and H_2O. *J. Inorg. Biochem.* **98**, 161-166 (2004).

25 XGBoost models for electrocatalytic conversion of CO_2 to glycerol. GitHub. https://github.com/fbhuiyan2/XGBoost-models-for-electrocatalytic-conversion-of-CO2-to-glycerol

26 Zhan, C. et al. Key intermediates and Cu active sites for CO_2 electroreduction to ethylene and ethanol. *Nat. Energy*, 1-12 (2024).

27 Jin, J. et al. Constrained C_2 adsorbate orientation enables CO-to-acetate electroreduction. *Nature* **617**, 724-729 (2023).

28 Hori, Y. et al. Formation of hydrocarbons in the electrochemical reduction of carbon dioxide at a copper electrode in aqueous solution. *J. Chem. Soc., Faraday Trans. 1* **85**, 2309-2326 (1989).

29 Sakamoto, N. et al. Dinuclear Cu(I) molecular electrocatalyst for CO_2-to-C_3 product conversion. *Nat. Catal.* **7**, 574-584 (2024).